EMPRESS. IX. Extremely Metal-poor Galaxies are Very Gas-rich Dispersion-dominated Systems: Will the James Webb Space Telescope Witness Gaseous Turbulent High-z Primordial Galaxies?

Yuki Isobe, Masami Ouchi, Kimihiko Nakajima, Shinobu Ozaki, Nicolas Bouché, John Wise, Yi Xu, Eric Emsellem, Haruka Kusakabe, Takashi Hattori, et al.

The Astrophysical Journal, 951:102 (18pp), 2023 July 10 https://doi.org/10.3847/1538-4357/accc87

EMPRESS. IX. Extremely Metal-poor Galaxies are Very Gas-rich Dispersion-dominated Systems: Will the James Webb Space Telescope Witness Gaseous Turbulent High-z Primordial Galaxies?

Yuki Isobe[1,2], Masami Ouchi[1,3,4], Kimihiko Nakajima[3], Shinobu Ozaki[3], Nicolas F. Bouché[5], John H. Wise[6], Yi Xu[1,7], Eric Emsellem[5,8], Haruka Kusakabe[9], Takashi Hattori[10], Tohru Nagao[11], Gen Chiaki[3], Hajime Fukushima[12], Yuichi Harikane[1,13], Kohei Hayashi[1,14,15], Yutaka Hirai[15,16], Ji Hoon Kim[17,18], Michael V. Maseda[19], Kentaro Nagamine[4,20,21], Takatoshi Shibuya[22], Yuma Sugahara[3,23], Hidenobu Yajima[12], Shohei Aoyama[1,24], Seiji Fujimoto[1,3,25,26,27], Keita Fukushima[20], Shun Hatano[28], Akio K. Inoue[23,29], Tsuyoshi Ishigaki[30], Masahiro Kawasaki[1,4], Takashi Kojima[1,2], Yutaka Komiyama[31], Shuhei Koyama[32], Yusei Koyama[10,28], Chien-Hsiu Lee[33], Akinori Matsumoto[1,2], Ken Mawatari[3], Takashi J. Moriya[3,34], Kentaro Motohara[3,32], Kai Murai[1], Moka Nishigaki[28], Masato Onodera[10,28], Yoshiaki Ono[1], Michael Rauch[35], Tomoki Saito[36], Rin Sasaki[30], Akihiro Suzuki[37], Tsutomu T. Takeuchi[38,39], Hiroya Umeda[1,2], Masayuki Umemura[12], Kuria Watanabe[28], Kiyoto Yabe[4], and Yechi Zhang[1,2]

[1] Institute for Cosmic Ray Research, The University of Tokyo, 5-1-5 Kashiwanoha, Kashiwa, Chiba 277-8582, Japan; isobe@icrr.u-tokyo.ac.jp
[2] Department of Physics, Graduate School of Science, The University of Tokyo, 7-3-1 Hongo, Bunkyo, Tokyo 113-0033, Japan
[3] National Astronomical Observatory of Japan, 2-21-1 Osawa, Mitaka, Tokyo 181-8588, Japan
[4] Kavli Institute for the Physics and Mathematics of the Universe (WPI), University of Tokyo, Kashiwa, Chiba 277-8583, Japan
[5] Univ Lyon, Univ Lyon1, ENS de Lyon, CNRS, Centre de Recherche Astrophysique de Lyon UMR5574, F-69230 Saint-Genis-Laval France
[6] Center for Relativistic Astrophysics, School of Physics, Georgia Institute of Technology, Atlanta, GA 30332, USA
[7] Department of Astronomy, Graduate School of Science, The University of Tokyo, 7-3-1 Hongo, Bunkyo, Tokyo 113-0033, Japan
[8] European Southern Observatory, Karl-Schwarzschild-Straße 2, D-85748 Garching, Germany
[9] Observatoire de Genéve, Université de Genéve, 51 Ch. des Maillettes, 1290 Versoix, Switzerland
[10] Subaru Telescope, National Astronomical Observatory of Japan, National Institutes of Natural Sciences (NINS), 650 North A'ohoku Place, Hilo, HI 96720, USA
[11] Research Center for Space and Cosmic Evolution, Ehime University, Bunkyo-cho 2–5, Matsuyama, Ehime 790-8577, Japan
[12] Center for Computational Sciences, University of Tsukuba, Ten-nodai, 1-1-1 Tsukuba, Ibaraki 305-8577, Japan
[13] Department of Physics and Astronomy, University College London, Gower Street, London WC1E 6BT, UK
[14] National Institute of Technology, Ichinoseki College, Hagisho, Ichinoseki, 021-8511, Japan
[15] Astronomical Institute, Tohoku University, 6-3 Aoba, Aramaki, Aoba-ku, Sendai, Miyagi 980-8578, Japan
[16] Department of Physics and Astronomy, University of Notre Dame, 225 Nieuwland Science Hall, Notre Dame, IN 46556, USA
[17] Astronomy Program, Department of Physics and Astronomy, Seoul National University, 1 Gwanak-ro, Gwanak-gu, Seoul 08826, Republic of Korea
[18] SNU Astronomy Research Center, Seoul National University, 1 Gwanak-ro, Gwanak-gu, Seoul 08826, Republic of Korea
[19] Department of Astronomy, University of Wisconsin-Madison, 475 N. Charter Street, Madison, WI 53706, USA
[20] Theoretical Astrophysics, Department of Earth & Space Science, Graduate School of Science, Osaka University, 1-1 Machikaneyama, Toyonaka, Osaka 560-0043, Japan
[21] Department of Physics & Astronomy, University of Nevada, Las Vegas, 4505 S. Maryland Parkway, Las Vegas, NV 89154-4002, USA
[22] Kitami Institute of Technology, 165 Koen-cho, Kitami, Hokkaido 090-8507, Japan
[23] Waseda Research Institute for Science and Engineering, Faculty of Science and Engineering, Waseda University, 3-4-1, Okubo, Shinjuku, Tokyo 169-8555, Japan
[24] Institute of Management and Information Technologies, Chiba University, 1-33, Yayoi-cho, Inage-ward, Chiba, 263-8522, Japan
[25] Cosmic DAWN Center, Denmark
[26] Niels Bohr Institute, University of Copenhagen, Lyngbyvej2, DK-2100, Copenhagen, Denmark
[27] Research Institute for Science and Engineering, Waseda University, 3-4-1 Okubo, Shinjuku, Tokyo 169-8555, Japan
[28] Department of Astronomical Science, SOKENDAI (The Graduate University for Advanced Studies), Osawa 2-21-1, Mitaka, Tokyo, 181-8588, Japan
[29] Department of Physics, School of Advanced Science and Engineering, Faculty of Science and Engineering, Waseda University, 3-4-1 Okubo, Shinjuku, Tokyo 169-8555, Japan
[30] Department of Physical Science and Materials Engineering, Faculty of Science and Engineering, Iwate University 3-18-34 Ueda, Morioka, Iwate 020-8550, Japan
[31] Department of Advanced Sciences, Faculty of Science and Engineering, Hosei University, 3-7-2 Kajino-cho, Koganei-shi, Tokyo 184-8584, Japan
[32] Institute of Astronomy, Graduate School of Science, The University of Tokyo, 2-21-1 Osawa, Mitaka, Tokyo 181-0015, Japan
[33] W.M. Keck Observatory, Kamuela, HI 96743, USA
[34] School of Physics and Astronomy, Faculty of Science, Monash University, Clayton, Victoria 3800, Australia
[35] Carnegie Observatories, 813 Santa Barbara Street, Pasadena, CA 91101, USA
[36] Nishi-Harima Astronomical Observatory, Centre for Astronomy, University of Hyogo, 407-2 Nishigaichi, Sayo, Sayo-gun, Hyogo 679-5313, Japan
[37] Research Center for the Early Universe, The University of Tokyo, 7-3-1 Hongo, Bunkyo, Tokyo 113-0033, Japan
[38] Division of Particle and Astrophysical Science, Nagoya University, Furo-cho, Chikusa-ku, Nagoya 464–8602, Japan
[39] The Research Center for Statistical Machine Learning, the Institute of Statistical Mathematics, 10-3 Midori-cho, Tachikawa, Tokyo 190–8562, Japan
Received 2022 June 9; revised 2023 April 2; accepted 2023 April 11; published 2023 July 6

Abstract

We present kinematics of six local extremely metal-poor galaxies (EMPGs) with low metallicities ($0.016–0.098\,Z_{\odot}$) and low stellar masses ($10^{4.7}–10^{7.6}M_{\odot}$). Taking deep medium/high-resolution ($R\sim7500$) integral-field spectra with 8.2 m Subaru, we resolve the small inner velocity gradients and dispersions of the

EMPGs with Hα emission. Carefully masking out substructures originating by inflow and/or outflow, we fit three-dimensional disk models to the observed Hα flux, velocity, and velocity dispersion maps. All the EMPGs show rotational velocities ($v_{\rm rot}$) of 5–23 km s^{-1} smaller than the velocity dispersions (σ_0) of 17–31 km s^{-1}, indicating dispersion-dominated ($v_{\rm rot}/\sigma_0 = 0.29$–$0.80 < 1$) systems affected by inflow and/or outflow. Except for two EMPGs with large uncertainties, we find that the EMPGs have very large gas-mass fractions of $f_{\rm gas} \simeq 0.9$–1.0. Comparing our results with other Hα kinematics studies, we find that $v_{\rm rot}/\sigma_0$ decreases and $f_{\rm gas}$ increases with decreasing metallicity, decreasing stellar mass, and increasing specific star formation rate. We also find that simulated high-z ($z \sim 7$) forming galaxies have gas fractions and dynamics similar to the observed EMPGs. Our EMPG observations and the simulations suggest that primordial galaxies are gas-rich dispersion-dominated systems, which would be identified by the forthcoming James Webb Space Telescope observations at $z \sim 7$.

Unified Astronomy Thesaurus concepts: Galaxy formation (595); Galaxy structure (622); Star formation (1569); Galaxy kinematics (602); Dwarf galaxies (416)

1. Introduction

Primordial galaxies characterized by low metallicities and low stellar masses are important to understand galaxy formation. Cosmological and hydrodynamical simulations (e.g., Wise et al. 2012; Yajima et al. 2022) have predicted that primordial galaxies at $z \sim 10$ would form in low-mass halos with halo masses of $\sim 10^8\,M_\odot$. Such simulated primordial galaxies at $z \gtrsim 7$ show low gas-phase metallicities of $\lesssim$1% of the solar abundance ($Z_\odot$), specific star formation rates (sSFRs) of $\sim$100 Gyr^{-1}, and low stellar masses of $\lesssim 10^6\,M_\odot$. Despite their scientific relevance, it is difficult to observe primordial galaxies due to their faintness. Isobe et al. (2022; hereafter Paper IV) have estimated an Hα flux of a primordial galaxy with $M_* = 10^6\,M_\odot$ as a function of the redshift, and demonstrated that even the currently best spectrographs such as Keck Low Resolution Imaging Spectrometer (LRIS) or Keck Multi-Object Spectrometer For Infra-Red Exploration (MOSFIRE) cannot observe the primordial galaxy at $z \gtrsim 0.5$ without any gravitational lensing magnification (e.g., Kikuchihara et al. 2020).

Kinematics of high-z primordial galaxies can provide us with a hint of what kind of mechanism (e.g., inflow/outflow) would impact early galaxy formation. We are still lacking a good handle on the detailed gas dynamical state, often quantified in broad terms by the relative level of rotation, via the $v_{\rm rot}/\sigma_0$ ratio (e.g., Förster Schreiber et al. 2009). Integral-field unit (IFU) observations (e.g., Wisnioski et al. 2015; Herrera-Camus et al. 2022) have reported that star-forming galaxies show $v_{\rm rot}/\sigma_0$ ratios decreasing from $v_{\rm rot}/\sigma_0 \sim 10$ to $\sim$2 with increasing redshift from $z \sim 0$ to 5.5, while such observations are currently limited to massive ($\sim 10^{10}\,M_\odot$) galaxies. It is important to directly determine whether low-mass ($\lesssim 10^6\,M_\odot$) primordial galaxies are truly dominated by dispersion.

Complementary to the high-z kinematics studies, some studies have reported $v_{\rm rot}/\sigma_0$ values of local galaxies with lower stellar masses. Local galaxies are advantageous for conducting deep observations with high spectral and spatial resolutions. The SHαDE survey (Barat et al. 2020) has made significant progress in extracting $v_{\rm rot}$ and σ_0 values of local dwarf galaxies with stellar masses down to $\sim 10^6\,M_\odot$. These observations suggest that the ratio $v_{\rm rot}/\sigma_0$ decreases down to $\lesssim$1 with decreasing M_* down to $\sim 10^6\,M_\odot$. However, the SHαDE galaxies have gas-phase oxygen metallicities[40] higher than $12 + \log({\rm O/H}) \sim 7.69$ that correspond to $Z \sim 0.1\,Z_\odot$ (Asplund et al. 2021), which are still $\gtrsim$1 dex higher than that of the simulated high-z primordial galaxy (Wise et al. 2012).

To understand the kinematic properties of chemically primordial galaxies, we investigate the Hα kinematics of local galaxies with $Z \leqslant 0.1\,Z_\odot$, which are often referred to as extremely metal-poor galaxies (e.g., Kunth 2000; Izotov et al. 2012), abbreviated as EMPGs (Kojima et al. 2020, hereafter Paper I). Although EMPGs become rarer toward lower redshifts (Morales-Luis et al. 2011), various studies have reported the presence of EMPGs in the local universe. Representative and well-studied EMPGs are SBS0335−052 (Izotov et al. 2009), AGC198691 (Hirschauer et al. 2016), Little Cub (Hsyu et al. 2017), DDO68 (Pustilnik et al. 2005), IZw18 (Izotov & Thuan 1998), and Leo P (Skillman et al. 2013). Izotov et al. (2018) have pinpointed J0811+4730 with a low metallicity of 0.02 $Z_\odot$.

Recently, a project called Extremely Metal-Poor Representatives Explored by the Subaru Survey (EMPRESS) has been launched (Paper I). EMPRESS aims to select faint EMPG photometric candidates from Subaru/Hyper Suprime-Cam (HSC; Miyazaki et al. 2018) deep optical ($i_{\rm lim} = 26$ mag; Aihara et al. 2019) images, which are $\sim$2 dex deeper than those of the Sloan Digital Sky Survey (SDSS). Conducting follow-up spectroscopic observations of the EMPG photometric candidates, EMPRESS has identified 12 new EMPGs with low stellar masses of $10^{4.2}$–$10^{6.6}\,M_\odot$ (Papers I, IV; Nakajima et al. 2022, hereafter Paper V; Xu et al. 2022, hereafter Paper VI). Remarkably, J1631+4426 has been reported to have a metallicity of 0.016 $Z_\odot$, which is the lowest metallicity identified so far (Paper I).

Including the 12 low-mass EMPGs found by EMPRESS, Paper V summarizes 103 local EMPGs identified so far whose metallicities are accurately measured with the direct-temperature method (e.g., Izotov et al. 2006). The 103 EMPGs show low metallicities of 0.016–0.1 $Z_\odot$, low stellar masses of $\sim 10^4$–$10^8\,M_\odot$, and high sSFRs of $\sim$1–400 Gyr^{-1} (Paper V). These features resemble the simulated primordial galaxy at $z \gtrsim 7$ (Wise et al. 2012), suggesting that EMPGs would be good local analogs of high-z primordial galaxies (but see also Isobe et al. 2021, hereafter Paper III).

This paper is the ninth paper of EMPRESS, reporting Hα kinematics of EMPGs observed with the Subaru/Faint Object Camera and Spectrograph (FOCAS) IFU (Ozaki et al. 2020) in a series of the Subaru Intensive Program entitled EMPRESS 3D (PI: M. Ouchi). So far, EMPRESS has released eight papers related to EMPGs, each of which reports the survey design (Paper I), high Fe/O ratios suggestive of massive stars (Kojima et al. 2021, hereafter Paper II; Paper IV), morphology

[40] Drawn from the SDSS MPA-JHU catalog (Brinchmann et al. 2004; Tremonti et al. 2004).

Table 1
Properties of the Six Observed EMPGs

#	Name	R.A. (hh:mm:ss)	Decl. (dd:mm:ss)	Redshift	$12 + \log(O/H)$	$\log(M_*)$ ($M_\odot$)	log(SFR) ($M_\odot$ yr^{-1})	log(sSFR) (Gyr^{-1})
(1)	(2)	(3)	(4)	(5)	(6)	(7)	(8)	(9)
1	J1631+4426	16:31:14.24	+44:26:04.43	0.0313	6.90 ± 0.03 (1)	5.9 (1)	−1.3 (1)	1.8
2	IZw18NW	09:34:02.03	+55:14:28.07	0.0024	7.16 ± 0.01 (2)	7.1 (3)	−1.4 (4)	0.5
3	SBS0335−052E	03:37:44.06	−05:02:40.19	0.0135	7.22 ± 0.07 (5)	7.6 (5)	−0.4 (4)	1.0
4	HS0822+3542	08:25:55.44	+35:32:31.92	0.0020	7.45 ± 0.02 (6)	4.6 (7)	−2.2 (8)	2.2
5	J1044+0353	10:44:57.79	+03:53:13.15	0.0130	7.48 ± 0.01 (6)	6.0 (7)	−0.9 (9)	2.1
6	J2115−1734	21:15:58.33	−17:34:45.09	0.0230	7.68 ± 0.01 (1)	6.6 (1)	0.3 (1)	2.7

Note. (1) Number. (2) Name. (3) R.A. in J2000. (4) decl. in J2000. (5) Redshift. (6) Metallicity. (7) Stellar mass. (8) Star formation rate based on the Hα luminosity. (9) Specific star formation rate.
References. (1) Paper I; (2) Izotov & Thuan (1998); (3) Annibali et al. (2013); (4) Thuan et al. (1997); (5) Izotov et al. (2009); (6) Kniazev et al. (2003); (7) This paper; (8) Kniazev et al. (2000); (9) Berg et al. (2016).

(Paper III), low-Z ends of metallicity diagnostics (Paper V), outflows (Paper VI), the shape of incident spectrum that reproduces high-ionization lines (Umeda et al. 2022, hereafter Paper VII), and the primordial He abundance (Matsumoto et al. 2022, hereafter Paper VIII).

This paper is organized as follows. Section 2 explains our observational targets. The observations are summarized in Section 3. Section 4 reports the Hα flux, velocity, and velocity dispersion maps of our targets. Our kinematic analysis is described in Section 5. Section 6 lists our results. We discuss kinematics of primordial galaxies in Section 7. Our findings are summarized in Section 8. Throughout this paper, magnitudes are in the AB system (Oke & Gunn 1983). We assume a standard ΛCDM cosmology with parameters of (Ω_m, Ω_Λ, H_0) = (0.3, 0.7, 70 km s^{-1} Mpc^{-1}). The solar metallicity $Z_\odot$ is defined by $12 + \log(O/H) = 8.69$ (Asplund et al. 2021).

2. Sample

We select six EMPGs visible on the observing nights (Section 3.1) and having relatively strong Hβ fluxes at a given metallicity so that we obtain kinematics of the EMPGs with high signal-to-noise (S/N) ratios. Details of the observational strategy will be reported in Xu et al. (2023). The six EMPGs consists of J1631+4426 (Paper I), IZw18 (e.g., Searle & Sargent 1972), SBS0335−052E (e.g., Izotov et al. 1997), HS0822+3542 (Kniazev et al. 2000), J1044+0353 (Papaderos et al. 2008), and J2115−1734 (Paper I).

We note that the four EMPGs other than J1631+4426 or J2115−1734 have radio and/or optical integral-field spectroscopy conducted by previous studies. IZw18 has H I observations with the Very Large Array (VLA; Lelli et al. 2012). SBS0335−052E also has VLA H I observations (Pustilnik et al. 2001) as well as Very Large Telescope Multi Unit Spectroscopic Explorer (MUSE) Hα observations with a spectral resolution of $R \sim 3000$ (Herenz et al. 2017). Our observations with FOCAS IFU are complementary to those previous observations of IZw18 and SBS0335−052E because of our higher spectral resolution ($R \sim 7500$, Section 3.1). HS0822+3542 and J1044+0353 have Hα observations with the 6 m Big Telescope Azimuthal (BTA)/Fabry–Perot interferometer having $R \sim 8000$ (Moiseev et al. 2010). FOCAS IFU can detect emission lines ∼2 times fainter than those of the Fabry–Perot interferometer with a similar spectral resolution.

The properties of the six observed EMPGs are listed in Table 1. The six EMPGs have low metallicities of $12 + \log(O/H) = 6.90$–7.68, low stellar masses of $\log(M_*/M_\odot) = 4.7$–7.6, and high specific star formation rates of $\log(\mathrm{sSFR}/\mathrm{Gyr}^{-1}) = 0.5$–$2.7$. These properties indicate that the six EMPGs are the best available analogs of primordial galaxies in the early universe. We emphasize that the six EMPGs include J1631+4426 having $12 + \log(O/H) = 6.90$ (Paper I), which is the lowest gas-phase metallicity among galaxies identified so far.

3. Observations and Data Analysis

3.1. Observations and Data Reduction

This section reports our spectroscopic observations with FOCAS IFU (Ozaki et al. 2020). FOCAS IFU is an IFU with an image slicer installed in FOCAS (Kashikawa et al. 2002) mounted on a Cassegrain focus of the Subaru 8.2 m telescope. The large diameter of the Subaru Telescope allows FOCAS IFU to perform deep integral-field spectroscopy with a 5σ limiting flux of $\sim 1 \times 10^{-17}$ erg s^{-1} cm^{-2} arcsec^{-2} (Ozaki et al. 2020).[41] The field of view (FoV) of FOCAS IFU is 13.″5 (slice length direction; hereafter, X direction)×10.″0 (slice width direction; hereafter, Y direction). The pixel scale in a reduced data cube is 0.″215 (X direction) and 0.″435 (Y direction).

We carried out spectroscopy with FOCAS IFU for the six EMPGs (Section 2). The observing nights were 2021 August 13, November 24, and December 13. We set pointing positions so that the whole structures of EMPGs are covered with single FoVs.

We used the mid/high-dispersion grism of VPH680 offering the spectral resolution of $R \sim 7500$. We took comparison frames of the ThAr lamp. We observed Feige67, HZ44, BD28, Feige110, and Feige34 as standard stars. All the nights were clear with seeing sizes of ∼0.″7.

We use a reduction pipeline software of FOCAS IFU[42] based on PyRAF (Tody 1986) and Astropy (Astropy Collaboration et al. 2013). The software performs bias subtraction, flat-fielding, cosmic-ray cleaning, sky subtraction, wavelength calibration with the comparison frames, and flux calibration. We estimate flux errors containing read-out noises and photon noises of sky and object emissions.

It should be noted that there remain systematic velocity differences among the slices even after the wavelength

[41] Under the assumptions of an 1 hr exposure and an extended source whose intrinsic line width is negligible with respect to the instrumental broadening.
[42] https://www2.nao.ac.jp/~shinobuozaki/focasifu/

calibration with the comparison frames. We conducted additional wavelength calibration with sky emission lines around observed wavelengths of Hα.

3.2. Flux, Velocity, and Velocity Dispersion Measurement

At all the spaxels, we fit the Hα lines using a single Gaussian function (+ constant) to measure the Hα fluxes, (relative) velocities, and velocity dispersions. We derive a line-spread function (LSF) by measuring widths of sky lines. A typical sky line has a FWHM of ∼0.8–1 Å. Assuming that both the Hα lines from the EMPGs and the sky lines agree well with the Gaussian function, we obtain the intrinsic velocity dispersions by subtracting the LSFs from the observed velocity dispersions quadratically. We confirm that the assumption is reasonable for most of the Hα lines and the sky lines other than some turbulent regions with multiple velocity components (Section 4).

We estimate the errors of the velocities and velocity dispersions by running the Monte Carlo simulations similar to the procedure of Herenz et al. (2016). We make 100 mock data cubes from our data cubes perturbed by the noise data cubes, and measure the velocities and velocity dispersions from each mock data cube. We regard the standard deviations of the derived velocities and velocity dispersions as the errors. The errors include the uncertainties of the LSFs, the additional wavelength calibration with the sky lines (Section 3.1), and the slit-width effect correction (see Section 3.3), because we perform these corrections using each mock data cube. Typical uncertainties of the velocity and velocity dispersion in each spaxel are ∼1.7 and ∼1.6 km s^{-1}, respectively. We self-consistently obtain the errors of the kinematic parameters in Sections 5.2 and 5.3 based on the 100 mock data cubes, in the same manner as we measure the errors of the velocities and velocity dispersions.

3.3. Slit-width-effect Correction

It should be noted that the observed velocities suffer from systematic wavelength shifts known as the slit-width effect (e.g., Bacon et al. 1995). Figure 1 illustrates the mechanism of the slit-width effect. The artificial wavelength shift is caused by a flux gradient in the Y direction (in each slice) that follows the dispersion (wavelength) axis (λ direction thereafter) on the CCD.

Assuming a 2D Gaussian function for the (spatial) flux profile (i.e., assuming a point source), Bacon et al. (1995) have derived the wavelength shifts originating from the slit-width effect. Considering that all our targets are extended and complex sources, we expanded the method to more flexible flux profiles. The wavelength shift $\lambda_{\rm shift}$ can be estimated from a barycenter of the flux intercepted by the slice as follows:

$$\lambda_{\rm shift} = \frac{\int_{-0.5w}^{0.5w} \lambda f(\lambda) {\rm d}\lambda}{\int_{-0.5w}^{0.5w} f(\lambda) {\rm d}\lambda}, \quad (1)$$

where w and $f(\lambda)$ are the slice width projected onto the CCD and the flux profile in the Y direction, respectively. Because the pseudo slit width is sampled by 4 pixels for each slice, w in units of Å is given by $w = 4d$, where d is a dispersion in units of Å pixel^{-1}.

We approximate $f(\lambda)$ by a quadratic function $f(\lambda) = a\lambda^2 + b\lambda + c$ so that the function form is determined by the three points (λ_{i-1}, f_{i-1}), (λ_i, f_i), and (λ_{i+1}, f_{i+1}) in Figure 1, where f_{i-1}, f_i, and f_{i+1} represent the fluxes of the $(i-1)$ th, ith, and $(i+1)$ th slices, respectively. In this case, $\lambda_{\rm shift}$ can be calculated as follows:

$$\lambda_{\rm shift} = \frac{\int_{-2d}^{2d} \lambda(a\lambda^2 + b\lambda + c){\rm d}\lambda}{\int_{-2d}^{2d} (a\lambda^2 + b\lambda + c){\rm d}\lambda} = \frac{4bd^2}{4ad^2 + 3c}. \quad (2)$$

We derive a, b, and c from the equations below:

$$a = \frac{f_{i-1} - 2f_i + f_{i+1}}{16d^2}$$
$$b = \frac{f_{i+1} - f_{i-1}}{4d}$$
$$c = f_i. \quad (3)$$

Using Equations (2) and (3), we obtain

$$\lambda_{\rm shift} = \frac{4(f_{i+1} - f_{i-1})}{f_{i-1} + 10f_i + f_{i+1}} d. \quad (4)$$

We infer from Equation (4) that high-dispersion dispersers make the slit-width effect weak. VPH680 has only $d = 0.22$ Å pixel^{-1}, which results in velocity shifts produced by the slit-width effect of only $\sim \pm 10$ km s^{-1} under the assumption of a seeing size of 0.″7. Although the velocity shift (∼10 km s^{-1}) is small, it is important to correct the slit-width effect because low-mass EMPGs are expected to have small velocity gradients (Section 4).

Panel (a) of Figure 2 shows an observed velocity map of one of the EMPGs (SBS0335−052E), and panel (b) shows the velocity shifts caused by the slit-width effect. A velocity map corrected for the slit-width effect is shown in panel (c).

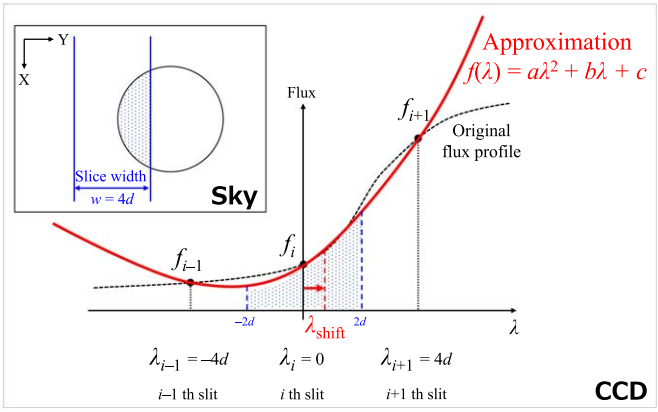

Figure 1. Explanation of the slit-width effect. The inset panel shows a schematic figure of an object on the celestial sphere. The X (Y) direction denotes the slice length (width) direction. The blue solid lines describe the position of the single slice. The light coming into the slice (blue shaded) is projected onto the CCD, where the Y direction in the sky is parallel to the wavelength (λ) direction on the CCD. The original spatial flux profile projected onto the CCD (black dashed curve) provides the fluxes of the $(i-1)$, i, and $(i+1)$th slices (f_{i-1}, f_i, and f_{i+1}, respectively). The original flux profile is assumed to be approximated by the quadratic function $f(\lambda) = a\lambda^2 + b\lambda + c$ (red solid curve) within an λ range from $-2d$ to $2d$. We estimate the systematic wavelength shift originating from the slit-width effect ($\lambda_{\rm shift}$) from a barycenter of the flux following $f(\lambda)$ intercepted by the slice.

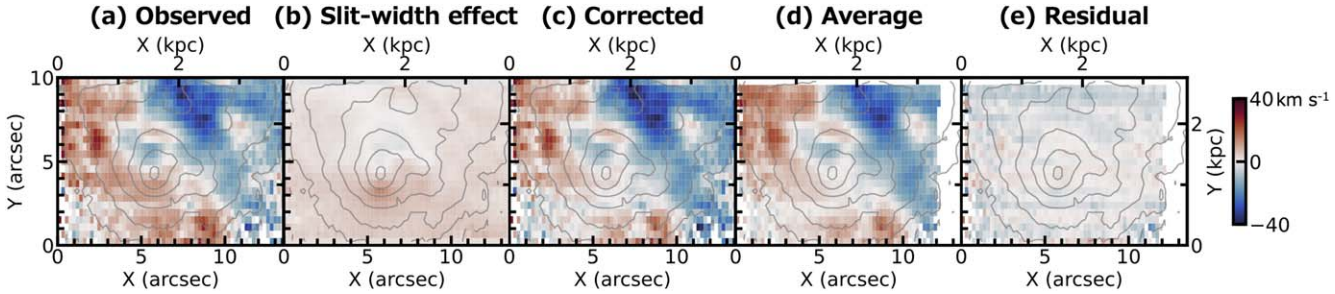

Figure 2. Confirmation of the slit-width effect correction using SBS0335−052E. (a) Observed velocity map. (b) Velocity shift generated by the slit-width effect. (c) Velocity map corrected for the slit-width effect. (d) Average of the two velocity maps whose position angles are different by 180°. (e) Residual of the corrected map and the average map. The gray contours illustrate S/N ratios in the order of 5, 10, 20, ... from the outside.

To test our slit-width effect correction, we observed SBS0335−052E with two frames whose position angles are different by 180°. We expect that an average of the two velocity maps obtained from the two frames cancel out the slit-width effect. Panel (d) of Figure 2 shows the average map, and panel (e) shows the residuals of the corrected map and the average map. The residuals are smaller than the velocity shifts caused by the slit-width effect. Figure 3 compares the residuals of the observed velocity map and the average map (i.e., residuals NOT corrected for the slit-width effect; left) and residuals of the corrected velocity map and the average map (i.e., residuals corrected for the slit-width effect; right). Figure 3 shows that the residuals become much smaller after slit-width-effect correction. The small residuals of $\sim \pm 5$ km s^{-1} also indicate that the corrected map agrees well with the average map. Thus, we conclude that our slit-width correction works well.

We evaluate the uncertainty of the slit-width effect correction by performing a Monte Carlo simulation based on flux errors. A typical value of the uncertainty is 0.3 km s^{-1}.

4. Flux, Velocity, and Dispersion Maps

Figure 4 summarizes the Hα flux, velocity, and velocity dispersion maps of the six EMPGs as well as *gri* images cut out of the FoV of FOCAS IFU. We note that only two EMPGs, #1 and #5 (i.e., J1631+4426 and J1044+0353), have images of the HSC-Subaru Strategic Program (SSP) Public Data Release (PDR) 3 (Aihara et al. 2022). The deep HSC images of the two EMPGs are shown in Figure 4, while the other *gri* images are taken from the Panoramic Survey Telescope and Rapid Response System (Pan-STARRS) catalog (Flewelling et al. 2020). We report the morphological and kinematic features of each EMPG below, checking the consistency with previous IFU studies.

#1 J1631+4426: The HSC *gri* image illustrates that J1631+4426 consists of a blue clump (indicated by the cyan arrow) and a white diffuse structure elongated from north to south (white arrow). We refer to the white structure as the "EMPG tail" (Paper III). The Hα flux map shows that the Hα flux of J1631+4426 is dominated by the blue clump, which indicates that star formation in J1631+4426 should mainly occur in that region. Paper I has confirmed that the blue clump has the very low metallicity of $12 + \log(\mathrm{O/H}) = 6.90$ (Section 2) based on the direct-temperature method, while the EMPG tail can have a metallicity even lower than the blue clump based on the [O III] λ5007/Hα ratio (Kashiwagi et al. 2021). The velocity map shows that the blue clump is discontinuously redshifted by

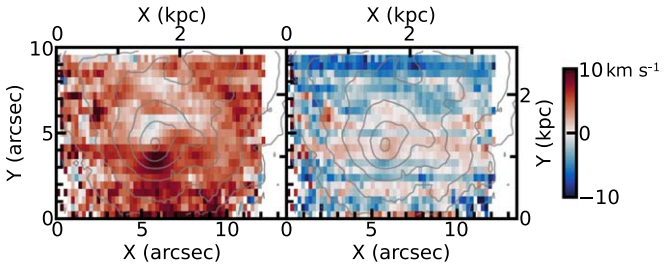

Figure 3. (Left) Residual of the observed velocity map and the average map in Figure 2. (Right) Residual of the corrected map and the average map, i.e., same as panel (e) in Figure 2, but for a smaller velocity range.

$\sim$20 km s^{-1} with respect to the EMPG tail, which indicates that the blue clump and the EMPG tail are not in the same kinematic structure. The blue clump itself shows a weak velocity gradient of $\sim$10 km s^{-1} from east to west, while the velocity dispersion is relatively high ($\sim$25 km s^{-1}).

#2 IZw18: IZw18 has two main blue clumps, IZw18 northwest (NW) and IZw18 southeast (SE), both of which have been confirmed to be EMPGs (Izotov & Thuan 1998). IZw18NW is blueshifted by $\sim$40 km s^{-1} with respect to IZw18SE (at around their flux peaks), consistent with the H I gas kinematics (Lelli et al. 2012). We thus think that IZw18NW and IZw18SE are not in the same kinematic structure. IZw18NW shows a complex morphokinematic structure. In the Hα flux map, we find that the arc-like structure indicated by the gray curve (Hα arc; Dufour & Hester 1990) has a velocity similar to that of IZw18NW, which indicates that the Hα arc and IZw18NW belong to the same kinematic structure. In the velocity map, we also identify a velocity structure that is redshifted by $\sim$20 km s^{-1} with respect to the flux peak of IZw18NW (red circle). The velocity structure has a relatively high velocity dispersion of $\sim$30 km s^{-1}, which implies that the structure is not settled. IZw18NW itself does not show a clear bulk rotation (i.e., not likely to be dominated by rotation).

#3 SBS0335−052E: The *gri* image shows that SBS0335−052E consists of a large blue clump (thick cyan arrow) and a western subclump (thin cyan arrow). In the velocity map, we confirm that SBS0335−052E has a redshifted ($\sim +20$ km s^{-1}) region northeast (red circle) and a blueshifted (~ -30 km s^{-1}) region northwest (blue circle). The redshifted and blueshifted regions seem connected to the northeast and north filaments identified with the wide-field MUSE Hα observations (Herenz et al. 2017), respectively. Both regions have relatively high velocity dispersions of $\sim$60 km s^{-1}, which agree with the

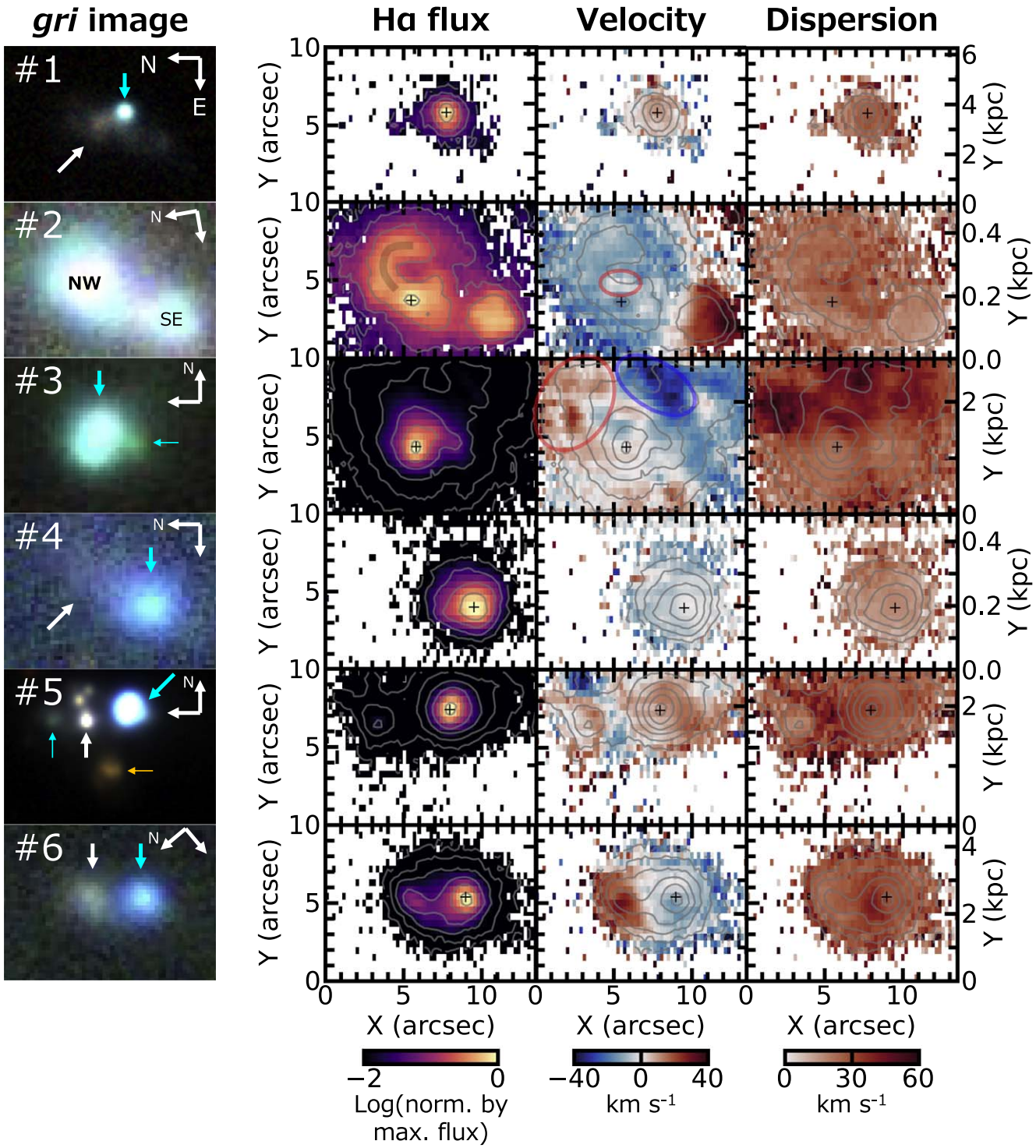

Figure 4. (Left) *gri* images of the six EMPGs cut out of the FoV of FOCAS IFU. The numbers correspond to those in Table 1. The images of #1 and #5 are drawn from the HSC-SSP PDR3 (Aihara et al. 2022), while the others are taken from the Pan-STARRS catalog (Flewelling et al. 2020). (Middle left) Observed Hα flux maps. The flux values in each flux map are normalized by the maximum flux value of each EMPG. The black crosses show the flux peaks. The gray contours are the same as those in Figure 2. (Middle right) Velocity maps showing relative velocities that fit well in the velocity range from -40 to 40 km s^{-1}. The velocity values are corrected for the slit-width effect (Section 3.3). (Right) Intrinsic velocity dispersion maps (Section 3.3).

scenario that the two structures are created by outflows (Herenz et al. 2017). The southern area of SBS0335−052E generally shows a relatively low velocity dispersion of $\sim$30 km s^{-1}, which indicates that the southern area is relatively settled. The southern area shows a bulk velocity gradient of $\sim$20 km s^{-1} from northwest to southeast.

#4 HS0822+3542: HS0822+3542 consists of a blue clump (cyan arrow) and a very diffuse EMPG tail elongated from southeast to northwest (white arrow). The Hα map indicates that the major star formation occurs in the blue clump. We find a very weak velocity gradient of $\sim$5 km s^{-1} in the blue clump from north to south. HS0822+3542 shows a high velocity

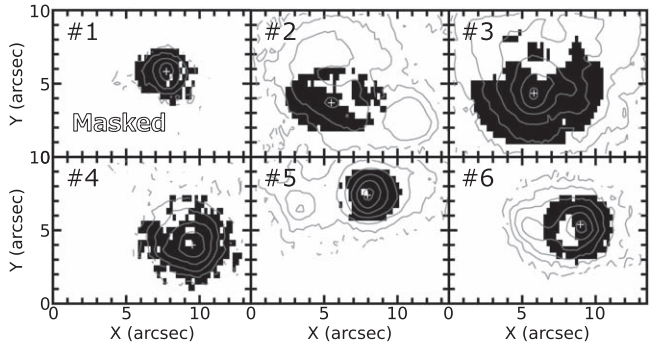

Figure 5. Mask map. The white regions correspond to the masked regions (Section 5.1).

dispersion of ∼20 km s^{-1}, which is comparable to the previous observations (Moiseev et al. 2010).

#5 J1044+0353: The deep HSC image shows that J1044 +0353 is composed of a western giant blue clump (thick cyan arrow), an eastern small blue clump (thin cyan arrow), and three white clumps between the two blue clumps (white arrow).[43] We regard the three white clumps as the EMPG tail. The Hα map indicates that major star formation occurs in the giant blue clump. We obtain similar velocity and velocity dispersion maps to Moiseev et al. (2010)'s result, while we show more clearly that the small blue clump emits Hα. We find that the two blue clumps are redshifted by ∼20 km s^{-1} with respect to the EMPG tail, which indicate that the two blue clumps and the EMPG tail are not in the same kinematic structure. We find that the giant blue clump has a weak velocity gradient of ∼20 km s^{-1} from southeast to northwest, while the velocity dispersion (∼30 km s^{-1}) is quite high.

#6 J2115−1734: J2115−1734 consists of a blue clump (cyan arrow) and a northeast EMPG tail (white arrow). The majority of star formation is likely to occur in the blue clump. The EMPG tail is redshifted by ∼40 km s^{-1} with respect to the blue clump. Although the observed velocity field continuously changes between the blue clump and the EMPG tail, J2115 −1734 shows a relatively high velocity dispersion of ∼40 km s^{-1} originating from two different velocity components. The blue clump itself has a weak velocity gradient of ∼20 km s^{-1} from northeast to southwest with a velocity dispersion of ∼30 km s^{-1}.

In summary, all six EMPGs look irregular and dominated by dispersion rather than rotation. Their rotation velocities are not likely to be significant. In Section 5, we analyze the kinematics of the EMPGs more quantitatively.

5. Kinematic Analysis

5.1. Masking

Below, we quantify the level of rotation of the EMPGs by assuming that those systems are represented by a single rotating disk. The dynamical center of the disk is thought to be located at the Hα flux peak of the main blue clump (IZw18NW for IZw18) under the assumptions of gas-mass dominance on the galactic scale (see, e.g., Herrera-Camus et al. 2022) and the empirical positive correlation between the gas-mass surface density $\Sigma_{\rm gas}$ and the star formation rate (SFR) surface density $\Sigma_{\rm SFR}$ (aka Kennicutt–Schmidt law; Kennicutt 1998). We confirm that these assumptions are reasonable by deriving the mass profile of each EMPG (Section 6.2). In the following analysis, we use only the region within the Kron radius of the main blue clump to remove the contamination from EMPG tails (IZw18SE for IZw18). We also mask spaxels with velocity dispersions higher than the flux-weighted 84th percentile of the distribution of the velocity dispersions because such regions are thought to be highly turbulent (Egorov et al. 2021). The white regions of Figure 5 show the masked regions.

5.2. Nonparametric Method

We calculate a shearing velocity $v_{\rm shear}$ of each EMPG, which is a nonparamteric kinematic property widely used in the literature (e.g., Law et al. 2009; Herenz et al. 2016). We derive $v_{\rm shear}$ from

$$v_{\rm shear} = \frac{1}{2}(v_{\rm max} - v_{\rm min}), \quad (5)$$

where $v_{\rm max}$ ($v_{\rm min}$) is the 95th (5th) percentile of the velocity distribution (Herenz et al. 2016). We note that high $v_{\rm shear}$ values do not necessarily imply the existence of rotation because different velocity components in the complex velocity fields can mimic rotation patterns at small scales. In this sense, $v_{\rm shear}$ can be regarded as an upper limit of the rotation velocity. The global velocity dispersion can be quantified by the flux-weighted median of the distribution of the velocity dispersions ($\sigma_{\rm med}$). We calculate the errors of the $v_{\rm shear}$ and $\sigma_{\rm med}$ values ($\Delta_{v_{\rm shear}}$ and $\Delta_{\sigma_{\rm med}}$, respectively) by running the Monte Carlo simulations explained in Section 3.2. We list $v_{\rm shear}$ and $\sigma_{\rm med}$ of the six EMPGs in Table 2. The medians of our $v_{\rm shear}/\Delta_{v_{\rm shear}}$ and $\sigma_{\rm med}/\Delta_{\sigma_{\rm med}}$ values are 22 and 73, respectively. These values are comparable to those of Herenz et al. (2016)'s observations, whose spectral resolutions and S/N ratios of Hα are similar to those of our observations. Herenz et al. (2016) report $v_{\rm shear}/\Delta_{v_{\rm shear}} \sim 22$ and $\sigma_{\rm med}/\Delta_{\sigma_{\rm med}} \sim 108$.

5.3. Parametric Method

We conduct detailed dynamical modeling with the 3D parametric code GalPaK$^{\rm 3D}$ (Bouché et al. 2015). Simultaneously constraining the morphological and kinematic properties from 3D data cubes, GalPaK$^{\rm 3D}$ provides the deprojected maximum rotational velocity ($v_{\rm rot}$) that is irrespective of the inclination. GalPaK$^{\rm 3D}$ also calculates σ_0 free from the velocity dispersions driven by the self gravity (e.g., Genzel et al. 2008) or mixture of the line-of-sight velocities. Because GalPaK$^{\rm 3D}$ does not support rectangular spaxels, we divide the spaxels in the *Y* direction based on the linear interpolation so that the pixel scale in the *Y* direction is the same as that in the *X* direction. We have 10 free parameters of XY coordinates of the disk center, systemic redshift, flux, inclination (i), position angle, effective radius of Hα ($r_{\rm e,H\alpha}$), turnover radius ($r_{\rm t}$), $v_{\rm rot}$, and intrinsic velocity dispersion σ_0. We assume that all six EMPGs have thick disks with rotation curves of the arctan profiles:

$$v(r) = v_{\rm rot}\sin(i)\frac{2}{\pi}\arctan(r/r_{\rm t}), \quad (6)$$

where r is a radius from the dynamical center. We note that i is determined by the axis ratio and the disk height, where the disk

[43] Using the 300B grism with a wide wavelength coverage, we detect [O III]$\lambda\lambda$ 4959,5007 lines at $z = 0.27$ from the southern red object (orange arrow). This means that the red object is a background galaxy and thus not related to J1044+0353.

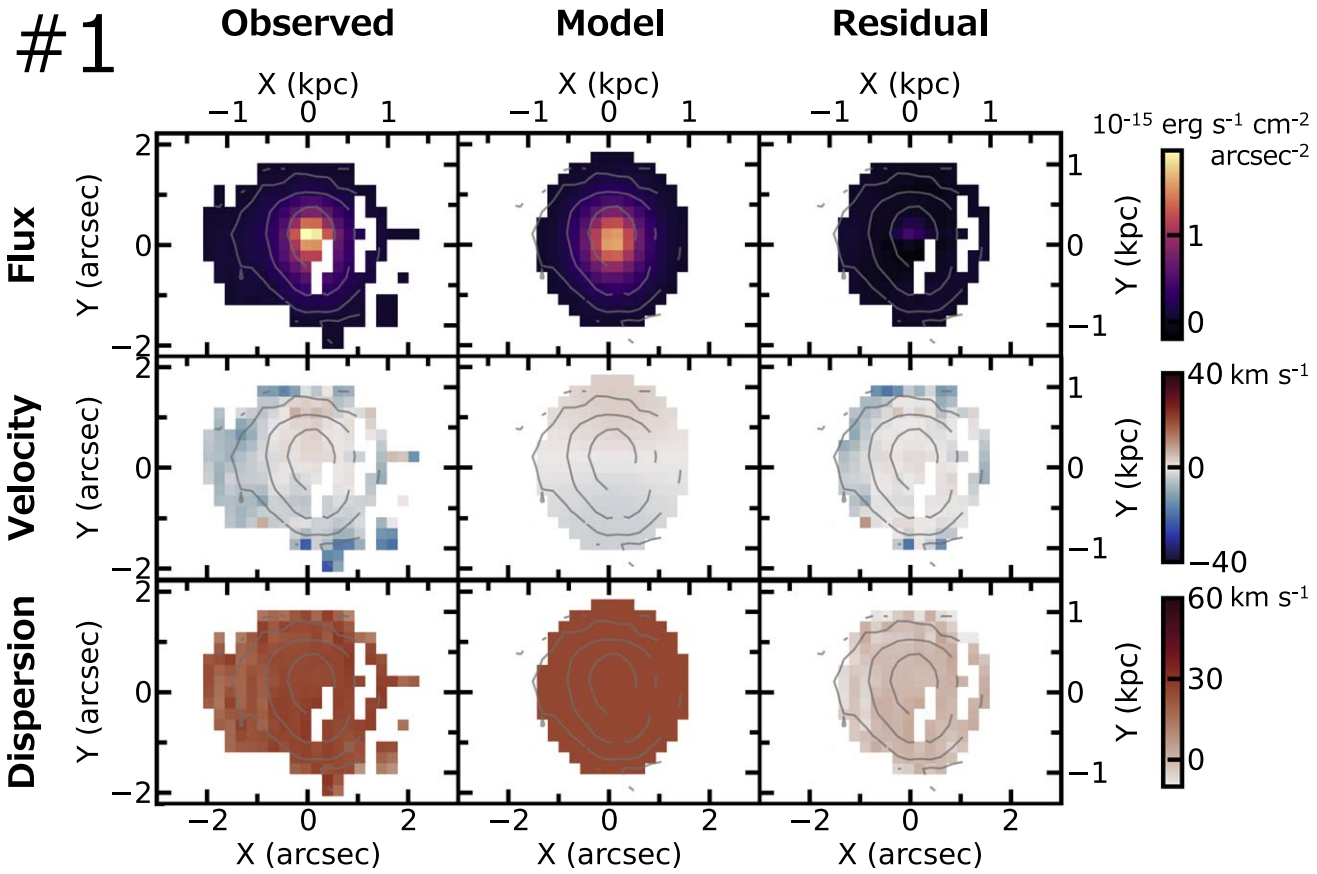

Figure 6. GalPaK^{3D} fitting of J1631+4426. The top, middle, and bottom panels show the Hα flux, velocity, and velocity dispersion maps, respectively. The left, center, and right panels illustrate the observed, model, and residual (=observed − model) maps, respectively. Note that the velocity maps in this figure denote the relative velocities with respect to the systemic redshift obtained with GalPaK^{3D} (Section 5.3).

Table 2
Kinematic Properties of the Six EMPGs

#	Name	$v_{\rm shear}$ km s^{-1}	$\sigma_{\rm med}$ km s^{-1}	$v_{\rm shear}/\sigma_{\rm med}$	$v_{\rm rot}$ km s^{-1}	σ_0 km s^{-1}	$v_{\rm rot}/\sigma_0$
(1)	(2)	(3)	(4)	(5)	(6)	(7)	(8)
1	J1631+4426	10.3 ± 1.3	25.6 ± 0.4	0.40 ± 0.05	7.9 ± 1.8	25.6 ± 0.3	0.31 ± 0.08
2	IZw18NW	7.7 ± 0.4	23.2 ± 0.5	0.33 ± 0.02	6.6 ± 2.9	22.9 ± 0.4	0.29 ± 0.13
3	SBS0335−052E	14.3 ± 0.4	24.6 ± 0.3	0.58 ± 0.02	19.7 ± 2.9	27.1 ± 0.3	0.73 ± 0.12
4	HS0822+3542	5.6 ± 0.7	16.9 ± 0.6	0.34 ± 0.07	4.5 ± 2.9	16.6 ± 0.5	0.27 ± 0.17
5	J1044+0353	5.5 ± 0.2	30.8 ± 0.3	0.18 ± 0.01	14.8 ± 4.2	31.4 ± 0.3	0.47 ± 0.14
6	J2115−1734	9.8 ± 0.4	29.7 ± 0.2	0.33 ± 0.01	23.4 ± 8.4	29.3 ± 0.1	0.80 ± 0.30

Note. (1) Number. (2) Name. (3) Shearing velocity. (4) Median velocity dispersion. (5) $v_{\rm shear}/\sigma_{\rm med}$. (6) Rotation velocity. (7) Intrinsic velocity dispersion. (8) $v_{\rm rot}/\sigma_0$.

height of the thick-disk model is fixed to $0.15 r_{\rm e,H\alpha}$ (Bouché et al. 2015). We also assume that the surface-brightness (SB) profiles follow Sérsic profiles with Sérsic indices $n = 1$, which are inferred from i-band SB profiles (Paper III). We have confirmed that these assumptions do not change $v_{\rm rot}$ and σ_0 much. We also use a point-spread function (PSF) obtained from standard stars with a Moffat profile whose FWHM and power index are $0\farcs7$ and $2\farcs5$, respectively. Figure 6 summarizes the fitting results. Table 2 lists the kinematic properties extracted by the GalPaK^{3D} analysis. We estimate the errors of the $v_{\rm rot}$ and σ_0 values by carrying out Monte Carlo simulations (Section 3.2). We note that $v_{\rm rot}$ can be regarded as an upper limit of the actual rotation velocity because the small-scale velocity differences in the complex velocity field can mimic rotation patterns (see also Section 5.2).

5.4. Mass Profile

The best-fit disk models obtained in Section 5.3 provide an estimate of the radial profiles for dynamical masses $M_{\rm dyn}$. The dynamical mass $M_{\rm dyn}$ is expected to be a sum of the stellar mass M_*, gas mass $M_{\rm gas}$, dark-matter (DM) mass $M_{\rm DM}$, and dust mass $M_{\rm dust}$. Note that $M_{\rm dust}$ is negligible in all six EMPGs because of their low $E(B-V)$ values (e.g., Paper I). Hereafter, we derive the radial profiles of $M_{\rm dyn}$, M_*, $M_{\rm gas}$, and $M_{\rm DM}$.

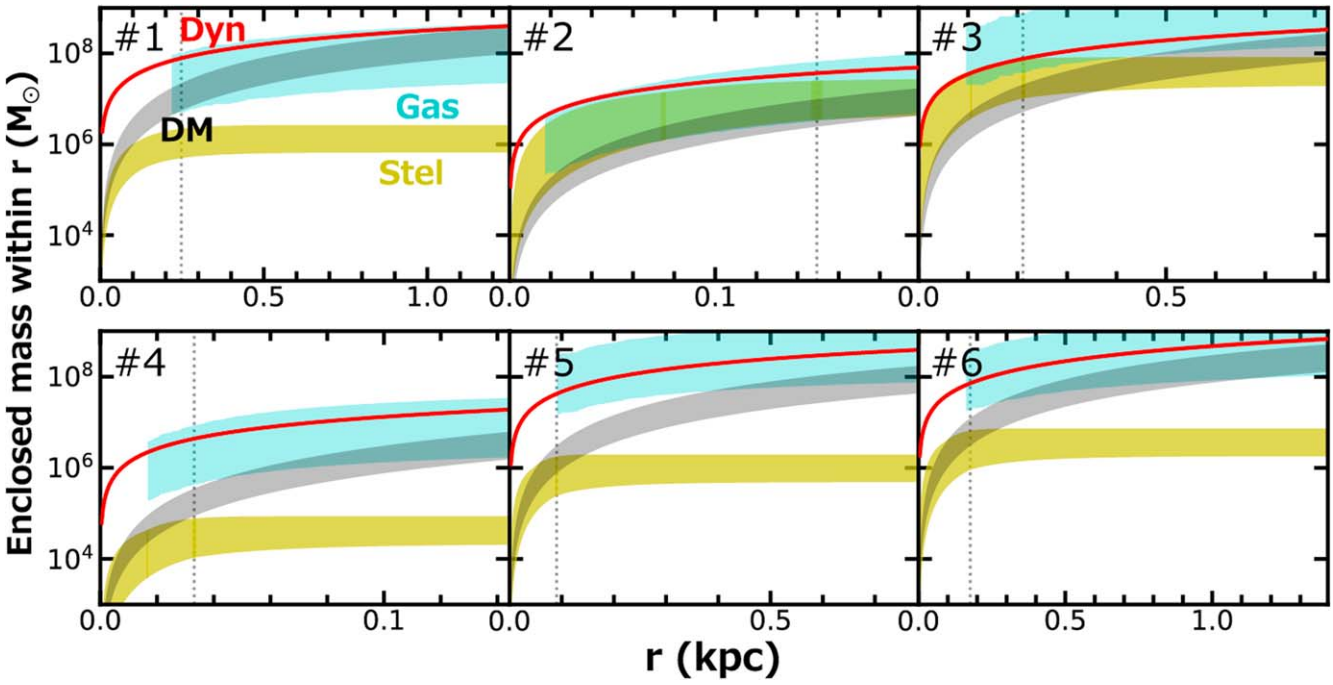

Figure 7. Enclosed mass profiles of the six EMPGs. The red, yellow, cyan, and black curves represent the dynamical, stellar, gas, and dark-matter mass profiles, respectively. The vertical dotted lines show $r_{e,H\alpha}$. The edge of the plots correspond to the outer most radii used for the kinematic analysis.

5.4.1. Dynamical Mass Profile

We derive M_{dyn} enclosed within a radius r from the equation

$$M_{dyn}(<r) = 2.33 \times 10^5 \left(\frac{r}{\mathrm{kpc}}\right) \times \left[\left(\frac{v(r)}{\mathrm{km\ s^{-1}}}\right)^2 + 2\left(\frac{\sigma_0}{\mathrm{km\ s^{-1}}}\right)^2\right] M_\odot \quad (7)$$

under the assumption of virial equilibrium. Figure 7 presents mass profiles of all six EMPGs. The red curves correspond to $M_{dyn}(<r)$. The dynamical masses within r_e are listed in Table 4.

5.4.2. Stellar Mass Profile

The stellar masses of four out of the six EMPGs (J1631+4426, J2115−1734, IZw18NW, and SBS0335−052E) are drawn from the literature (Paper I; Izotov & Thuan 1998; Izotov et al. 2009). For the other two targets (J1044+0353 and HS0822+3542), we provide here an estimate of their stellar mass.

We use the spectral energy distribution (SED) interpretation code of BEAGLE (Chevallard & Charlot 2016). The BEAGLE code calculates both the stellar continuum and the nebular emission using the stellar population synthesis code (Bruzual & Charlot 2003) and the nebular emission library of Gutkin et al. (2016) that are computed with the photoionization code CLOUDY (Ferland et al. 2013). We fit the SED models to the SDSS *ugriz*-band photometries (DR16; Ahumada et al. 2020). We run the BEAGLE code with four free parameters, namely, the maximum stellar age t_{max}, stellar mass M_*, ionization parameter U, and V-band optical depth τ_V whose parametric ranges are the same as those adopted in Papers III and IV. We fix the metallicities Z to be the gas-phase metallicities $12 + \log(O/H)$ listed in Table 1. We also assume a constant SFH and the Chabrier (2003) IMF in the same manner as Papers III and IV.

Table 3
Morphological and Additional kinematic Properties of the Six EMPGs

#	Name	$r_{e,H\alpha}$ (pc)	i (deg)	P.A. (deg)	r_t (pc)
(1)	(2)	(3)	(4)	(5)	(6)
1	J1631+4426	248	44	178	61
2	IZw18NW	149	72	68	339
3	SBS0335−052E	211	25	320	258
4	HS0822+3542	33	41	91	1.1
5	J1044+0353	90	41	159	106
6	J2115−1734	176	43	222	387

Note. (1) Number. (2) Name. (3) Hα effective radius. (4) Inclination. (5) Position angle. (6) Turnover radius.

We note that we conduct the SED fitting with almost the same setting as that of Paper I for J1631+4426 and J2115−1734, except for Z and τ_V. In Paper I, Z is treated as a free parameter, and τ_V is fixed to be 0, while it has no impact on M_* of J1631+4426 and J2115−1734 because both EMPGs are dust poor (Paper I). We also confirm that the stellar masses of the six EMPGs are different only by $\lesssim$0.3 dex from those derived from i-band magnitudes based on the same mass-to-light ratio. We include this systematic error of 0.3 dex into the total error of the M_* profile.

To obtain M_* profiles, we assume that azimuthally averaged M_* distributions of the EMPGs follow Sérsic profiles. J1631+4426 has an i-band effective radius ($r_{e,i}$) of 137^{+9}_{-7} pc and an i-band Sérsic index (n_i) of $1.08^{+0.15}_{-0.13}$ (Paper III). Because the i-band surface-brightness distribution is expected to trace the M_* distribution well (Paper III), we assume that J1631+4426 has a stellar effective radius ($r_{e,*}$) and a stellar Sérsic index (n_*) equal to $r_{e,i}$ and n_i, respectively. We also assume that the other

Table 4
Enclosed Dynamical, Stellar, Gas, and DM Masses, Gas-mass Fraction, and Toomre Q

#	Name	$\log(M_{\rm dyn}(<r_{\rm e,H\alpha}))$ $M_\odot$	$\log(M_*(<r_{\rm e,H\alpha}))$ $M_\odot$	$\log(M_{\rm gas}(<r_{\rm e,H\alpha}))$ $M_\odot$	$\log(M_{\rm DM}(<r_{\rm e,H\alpha}))$ $M_\odot$	$f_{\rm gas}$	Q
(1)	(2)	(3)	(4)	(5)	(6)	(7)	(8)
1	J1631+4426	7.90 ± 0.06	6.0 ± 0.3	$7.0^{+1.0}_{-0.3}$	7.1 ± 0.3	$0.91^{+0.06}_{-0.34}$	$5.1^{+2.1}_{-1.6}$
2	IZw18NW	7.56 ± 0.02	7.0 ± 0.3	$6.8^{+1.0}_{-0.3}$	6.7 ± 0.3	$0.42^{+0.38}_{-0.32}$	$11.6^{+56.7}_{-3.2}$
3	SBS0335−052E	7.88 ± 0.02	7.4 ± 0.3	$7.9^{+1.0}_{-0.3}$	7.0 ± 0.3	$0.74^{+0.17}_{-0.51}$	$2.6^{+4.7}_{-0.7}$
4	HS0822+3542	6.64 ± 0.03	4.4 ± 0.3	$5.9^{+1.0}_{-0.3}$	5.2 ± 0.3	$0.97^{+0.03}_{-0.07}$	$5.4^{+0.2}_{-2.5}$
5	J1044+0353	7.63 ± 0.07	5.8 ± 0.3	$7.5^{+1.0}_{-0.3}$	6.2 ± 0.3	$0.98^{+0.01}_{-0.09}$	$3.1^{+3.2}_{-0.0}$
6	J2115−1734	7.86 ± 0.06	6.4 ± 0.3	$7.6^{+1.0}_{-0.3}$	6.8 ± 0.3	$0.94^{+0.04}_{-0.18}$	$1.9^{+0.5}_{-0.6}$

Note. (1) Number. (2) Name. (3) Dynamical mass enclosed in $r_{\rm e,H\alpha}$. (4) Stellar mass enclosed in $r_{\rm e,H\alpha}$. (5) Gas mass enclosed in $r_{\rm e,H\alpha}$. (6) Dark-matter mass enclosed in $r_{\rm e,H\alpha}$. (7) Gas-mass fraction within $r_{\rm e,H\alpha}$. (8) Global Toomre Q parameter (Section 7.2).

five EMPGs have $r_{\rm e,*}$ within the range from $r_{\rm e,H\alpha}/2$ to $r_{\rm e,H\alpha}$ because $r_{{\rm e},i}$ of J1631+4426 is ∼2 times smaller than $r_{\rm e,H\alpha}$ of J1631+4426 (see Table 3).[44] We confirm that the assumed $r_{\rm e,*}$ of the five EMPGs are comparable to $r_{{\rm e},i}$ of EMPGs (Paper III). The five EMPGs are assumed to have n_* within the range from 0.7 to 1.7 inferred from the typical n_i value of EMPGs (Paper III). We include these uncertainties of $r_{\rm e,*}$ and n_* into the error of the M_* profile. The yellow shaded regions in Figure 7 represent cumulative M_* profiles with their uncertainties. The stellar masses within $r_{\rm e}$ are listed in Table 4.

5.4.3. Gas Mass Profile

We obtain $M_{\rm gas}$ distributions from the Hα flux distributions, using the Kennicutt–Schmidt law (Section 5.1). However, observational studies (e.g., Shi et al. 2014) have reported that some EMPGs have $\Sigma_{\rm gas}$ values ∼1 dex larger than those inferred from the Kennicutt–Schmidt law, which can be interpreted as the lack of metals suppressing efficient gas cooling and succeeding star formation (e.g., Ostriker et al. 2010; Krumholz 2013). Given the uncertainty of the Kennicutt–Schmidt law at the low-metallicity end, we add this 1 dex upper error to the original scatter of the Kennicutt–Schmidt law (∼0.3 dex; Kennicutt 1998). The cyan shaded regions in Figure 7 indicate cumulative $M_{\rm gas}$ profiles with their uncertainties. We note that the H I observations of Lelli et al. (2012) and Pustilnik et al. (2001) have reported that IZw18NW and SBS0335−052E have $M_{\rm gas} \sim 1 \times 10^8$ and $\sim 1 \times 10^9\,M_\odot$ within wide scales of ∼0.2 and ∼3 kpc, respectively, which are consistent with the extrapolations of the $M_{\rm gas}$ profiles that we derive. The gas masses within $r_{\rm e}$ are listed in Table 4. We obtain gas-mass fractions at $r_{\rm e,H\alpha}$ from the following equation $f_{\rm gas} = M_{\rm gas}(<r_{\rm e,H\alpha})/[M_{\rm gas}(<r_{\rm e,H\alpha}) + M_*(<r_{\rm e,H\alpha})]$.

5.4.4. Dark-matter Mass Profile

We estimate $M_{\rm DM}$ profiles under the assumption that the $M_{\rm DM}$ (density) profile follows the Navarro–Frenk–White (NFW) profile (Navarro et al. 1996). At the virial radius r_{200} within which the spherically averaged mass density is 200 times the critical density $\rho_{\rm c}$, the NFW profile can be described by

$$\rho(r) = \rho_{\rm c} \frac{\delta}{c_{200} x (1 + c_{200} x)^2}, \tag{8}$$

where

$$\delta = \frac{200}{3} \frac{c_{200}^3}{\ln(1 + c_{200}) - c_{200}/(1 + c_{200})} \tag{9}$$

and $x = r/r_{200}$. The concentration parameter c_{200} is defined as the ratio $r_{200}/r_{\rm d}$ controlling where the slope equals −2 as it changes from −3 at large radii to a central value of −1. We obtain r_{200} from the virial mass M_{200} using the equation

$$r_{200} = \left[\frac{3 M_{200}}{4\pi (200 \rho_{\rm c})} \right]^{1/3}. \tag{10}$$

We derive M_{200} from an empirical stellar-to-halo mass ratio of dwarf galaxies (Brook et al. 2014) of

$$M_{200} = 7.96 \times 10^7 \left(\frac{M_*}{M_\odot} \right)^{1/3.1} M_\odot. \tag{11}$$

We note that the scatter of the observed stellar-to-halo mass ratios of dwarf galaxies around Equation (11) is ∼0.3 dex (Prole et al. 2019). We include this uncertainty into the error of the $M_{\rm DM}$ profile. We also obtain c_{200} from M_{200} using a halo mass–concentration relation for the Planck cosmology (Dutton & Macciò 2014):

$$\log(c_{200}) = 0.905 - 0.101 \log(M_{200}/10^{12} h^{-1} M_\odot), \tag{12}$$

where $h = H_0/(100\,{\rm km\,s^{-1}\,Mpc^{-1}})$.[45] The gray shaded regions in Figure 7 denote the $M_{\rm DM}$ profiles with their uncertainties. The DM masses within $r_{\rm e}$ are listed in Table 4.

6. Results

6.1. Rotation and Dispersion

Table 2 summarizes $v_{\rm shear}$, $\sigma_{\rm med}$, $v_{\rm rot}$, and σ_0 of the six EMPGs. Note that $v_{\rm shear}$ and $\sigma_{\rm med}$ ($v_{\rm rot}$ and σ_0) are based on the nonparametric (parametric) method explained in Section 5.2 (5.3). We find that all six EMPGs have low $v_{\rm shear}$ (5.5–14.3 km s^{-1}), high $\sigma_{\rm med}$ (16.9–30.8 km s^{-1}), and thus low $v_{\rm shear}/\sigma_{\rm med}$ (0.18–0.58). Regarding SBS0335−052E, Herenz et al. (2017) also obtained $v_{\rm shear}/\sigma_{\rm med} = 0.68$, which is close to our measurement of $v_{\rm shear}/\sigma_{\rm med} = 0.58 \pm 0.02$. The six EMPGs also have low $v_{\rm rot}$ (4.5–23.4 km s^{-1}), high σ_0 (16.6–31.4 km s^{-1}), and low $v_{\rm rot}/\sigma_0$ (0.27–0.80). Using the two different

[44] This result also suggests that EMPGs would have Hα halos as discussed in Herenz et al. (2017).

[45] We use $h = 0.7$ for consistency with our analysis based on the standard ΛCDM cosmology (Section 1), while we confirm that $h = 0.67$ based on the Planck cosmology does not change our conclusion.

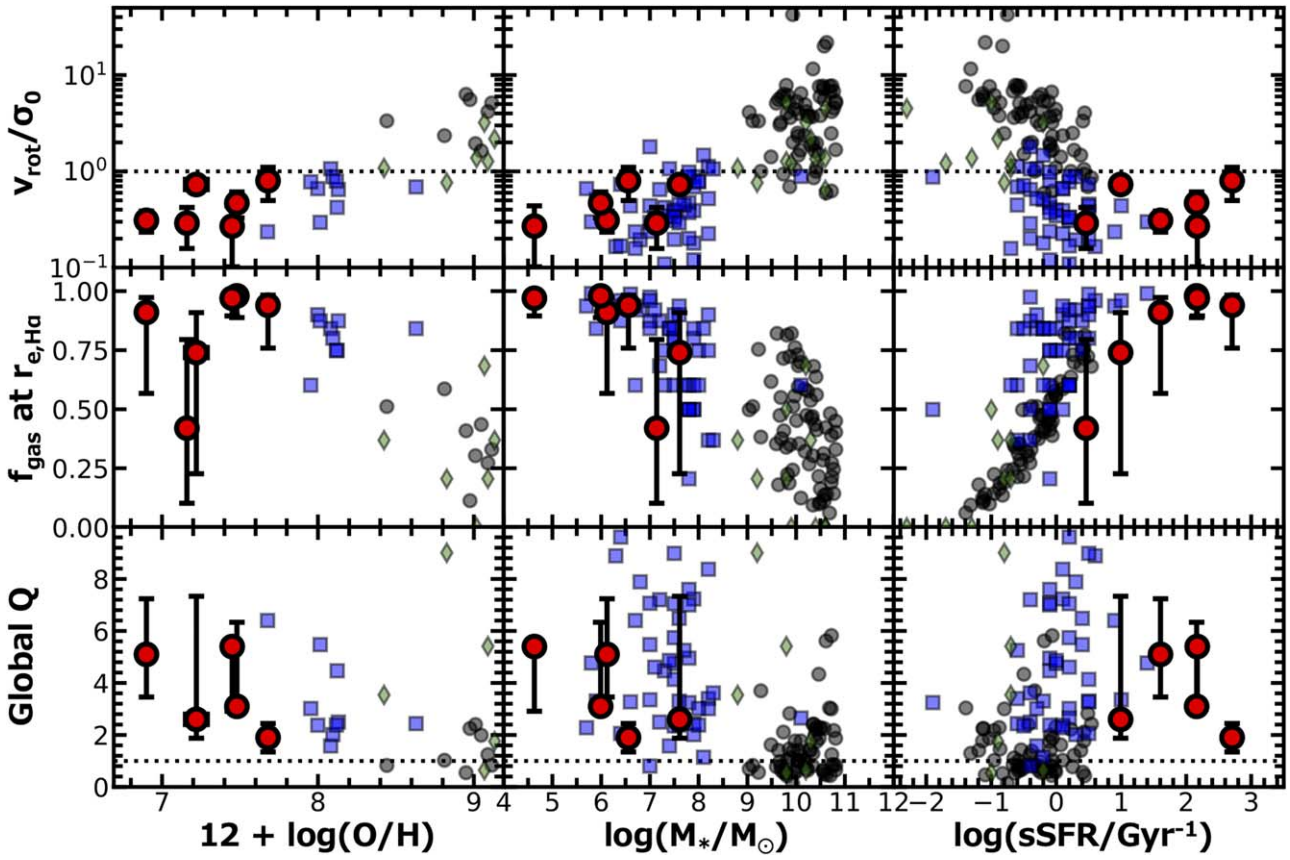

Figure 8. Diagrams of v_{rot}/σ_0, f_{gas}, and global Q as functions of 12 + log(O/H), M_*, and sSFR. The red circles represent the EMPGs, while the blue squares, the green diamonds, and the black circles indicate the SHαDE (Barat et al. 2020), SAMI (Barat et al. 2019), and DYNAMO galaxies (Green et al. 2014), respectively. Because IZw18NW has the large uncertainty of the global Q (see Table 4), we exclude the data point of this EMPG from the bottom panels.

methods, we confirm that all six EMPGs are dominated by dispersion (i.e., v_{shear}/σ_{med}, $v_{rot}/\sigma_0 < 1$).

The top left panel of Figure 8 shows v_{rot}/σ_0 values of the six EMPGs (red circle) as a function of the metallicity. We compare our results with other surveys of Hα kinematics of star-forming dwarf galaxies (SHαDE; Barat et al. 2020) and star-forming galaxies (SAMI; Barat et al. 2019; DYNAMO; Green et al. 2014), whose metallicities are drawn from the SDSS MPA-JHU catalog (Brinchmann et al. 2004; Tremonti et al. 2004). The SHαDE, SAMI, and DYNAMO galaxies have 12 + log(O/H) $\sim$ 8–9. We find that v_{rot}/σ_0 decreases with decreasing 12 + log(O/H). The top middle and top right panels of Figure 8 show v_{rot}/σ_0 as a function of M_* and the sSFR, respectively. The SFRs are derived from the Hα luminosity. M_* and the sSFR potentially have uncertainties of $\sim$0.3 dex under different assumptions such as initial mass functions (see Section 5.4.2). Although it should be noted that the EMPGs are biased toward lower metallicities, we also find that v_{rot}/σ_0 decreases as M_* decreases and sSFR increases. These results suggest that galaxies in earlier stages of the formation phase may have lower v_{rot}/σ_0.

6.2. Mass Fraction

Figure 7 summarizes the radial profiles of M_{dyn} (red), M_* (yellow), M_{gas} (cyan), and M_{DM} (black). We find that four EMPGs other than IZw18NW and SBS0335−052E have M_* profiles $\sim$2 dex below the M_{dyn} profiles within radii up to several times $r_{e,H\alpha}$, which means that the four EMPGs are dominated by M_{gas} or M_{DM} on galactic scales. On the other hand, IZw18NW and SBS0335−052E have M_* profiles comparable to the M_{dyn} profiles. We also find that the M_{dyn} profiles of all six EMPGs can be explained by the M_{gas} profiles within the uncertainties (see Section 5.4.3). We confirm that the M_{DM} profiles of all six EMPGs are $\sim$1 dex below the M_{dyn} profiles within radii up to several times $r_{e,H\alpha}$. We thus conclude that the masses of the four EMPGs except for IZw18NW and SBS0335−052E are dominated by M_{gas} on galactic scales. We note that IZw18NW and SBS0335−052E indeed have large M_{gas} values of $\sim 1 \times 10^8$ and $\sim 1 \times 10^9\,M_\odot$ inferred from the H I observations within $\sim$0.2 and $\sim$3 kpc, respectively (Section 5.4.3). Within these larger scales, we can say that both IZw18NW and SBS0335−052E are gas rich (i.e., $f_{gas} \sim 1$). This conclusion is consistent with those in Pustilnik et al. (2020a, 2020b, 2021) based on H I observations. It should also be noted that Equations (10) and (11) suggest that EMPGs with $\sim 10^6\,M_\odot$ have $M_{200} \sim 7 \times 10^9\,M_\odot$ at $r_{200} \sim 30$ kpc, whereas we can only observe the area within at most $\sim$1 kpc. Therefore, it is natural that M_{DM} has negligible effects on the mass profile in this study.

The middle left panel of Figure 8 shows f_{gas} of the six EMPGs as a function of the metallicity. Except for IZw18NW and SBS0335−052E with large f_{gas} uncertainties, we find that the EMPGs are gas rich with high f_{gas} values of $\sim$0.9–1.0. Comparing with the literature, we find that galaxies with lower metallicities tend to have higher f_{gas} values. The f_{gas} values also

increase at lower M_* and higher sSFRs. These results indicate that galaxies in the earlier formation phase would have higher $f_{\rm gas}$, which are consistent with previous observations (e.g., Maseda et al. 2014) as well as models of galaxy formation based on the ΛCDM model (e.g., Geach et al. 2011). It should be noted that $M_{\rm gas}$ of the SHαDE and DYNAMO galaxies are estimated from the Kennicutt–Schmidt law (i.e., correlation between $\Sigma_{\rm SFR}$ and $\Sigma_{\rm gas}$) in a similar way as our analysis (see Section 5.4.3). Thus, it is natural that we find a tight correlation between the sSFR and $f_{\rm gas}$.

7. Discussion

7.1. Origin of Low $v_{\rm rot}/\sigma_0$

In Section 6.1, we report that all six EMPGs have low $v_{\rm rot}/\sigma_0 < 1$. We also find that $v_{\rm rot}/\sigma_0$ decreases with decreasing $12 + \log({\rm O/H})$, decreasing M_*, and increasing sSFR (Figure 8). Below, we investigate three well-discussed contributors (e.g., Glazebrook 2013; Barat et al. 2020) to such a low $v_{\rm rot}/\sigma_0 < 1$.

7.1.1. Thermal Expansion

The first possible contributor to the low $v_{\rm rot}/\sigma_0$ is the thermal expansion of H II regions (e.g., Krumholz et al. 2018; Fukushima & Yajima 2021, 2022). We estimate a velocity dispersion of the thermal expansion ($\sigma_{\rm th}$) from the line-of-sight component of the Maxwellian velocity distribution ($\sigma_{\rm th} = \sqrt{kT_{\rm e}/m}$; e.g., Chávez et al. 2014; Pillepich et al. 2019), where k, $T_{\rm e}$, and m represent the Boltzmann constant, the electron temperature, and the hydrogen mass, respectively. We obtain $\sigma_{\rm th} = 9.1$ km s^{-1} under the assumption of $T_{\rm e} = 10,000$ K, which is consistent with the typical electron temperature of O II (i.e., H II) regions of the EMPGs (e.g., Paper I). Subtracting $\sigma_{\rm th}$ from σ_0 quadratically, we obtain velocity dispersions that are free from thermal line broadening ($\sigma_{\rm no\_therm} = 14$–$30$ km s^{-1}). We confirm that $v_{\rm rot}/\sigma_{\rm no\_therm}$ values are still lower than unity (0.31–0.84) for all six EMPGs. We thus conclude that thermal expansion cannot explain $v_{\rm rot}/\sigma_0 < 1$.

7.1.2. Merger/Inflow

The second possible contributor are merger/inflow events (e.g., Glazebrook 2013). The merger (inflow) can raise velocity dispersions by tidal heating (releasing potential energies of infalling gas). This scenario can explain all the trends seen in Figure 8 because we can expect that both gas-rich minor merger and inflow would supply metal-poor gas and trigger succeeding starbursts. For J1631+4426, IZw18NW, SBS0335−052E, and J2115−1734 in particular, we find velocity differences from the EMPG tails (IZw18SE for IZw18NW) suggestive of a merger (Section 4).

7.1.3. Stellar Feedback

The third possible contributor is the stellar feedback (e.g., Lehnert et al. 2009). This includes supernovae (SNe) feedback (Dib et al. 2006) as well as stellar winds and the radiative pressure from young massive stars (Mac Low & Klessen 2004). Outflowing gas from SNe and/or young massive stars would raise velocity dispersions. This stellar feedback scenario can directly explain the decreasing trend between $v_{\rm rot}/\sigma_0$ and the sSFR (top right panel of Figure 8). Given the expectation that young galaxies (i.e., with high sSFRs) would have low $12 + \log({\rm O/H})$ and M_*, this scenario can indirectly reproduce the trend that $v_{\rm rot}/\sigma_0$ decreases with decreasing $12 + \log({\rm O/H})$ and M_*. IZw18NW, SBS0335−052E, and J1044+0353 especially show outflow signatures in the flux, velocity, and velocity dispersion maps (see Section 4), which imply the dominance of the stellar feedback. We thus conclude that the stellar feedback can also be one of the main contributors of $v_{\rm rot}/\sigma_0 < 1$ at the low-metallicity, low-M_*, and high-sSFR ends. Cosmological zoom-in simulations will provide a hint of what kind of feedback is the main contributor.

7.2. Toomre Q Parameter

To compare with other kinematic studies, we derive the Toomre Q parameter (Toomre 1964) of the EMPGs. In general, if the Q value of a rotating disk is greater than unity (i.e., $Q > 1$), the disk is thought to be gravitationally stable. On the other hand, the disk is gravitationally unstable if $Q < 1$. However, note that it is unclear if this criterion is applicable for the EMPGs because they may not have rotating disks (Section 4). An average of Q within a disk, the so-called global Q (e.g., Aumer et al. 2010), is calculated from the equation

$$Q = \frac{\sigma_0}{v_{\rm rot}} \frac{a}{f_{\rm gas}}, \tag{13}$$

where a is a parameter with values ranging from 1 to 2 depending on the gas distribution (Genzel et al. 2011). Here, we adopt $a = \sqrt{2}$ assuming the constant rotational velocity.

Table 4 lists the global Q of the six EMPGs. We find that all six EMPGs show $Q > 1$, albeit one of the six EMPGs (IZw18NW) has a large Q uncertainty. The bottom panels of Figure 8 illustrate the global Q of the EMPGs as a function of the metallicity (bottom left), M_* (bottom center), and the sSFR (bottom right), while we exclude IZw18NW due to its large Q uncertainty. We also find that the global Q increases with decreasing $12 + \log({\rm O/H})$, decreasing M_*, and increasing sSFR. However, the large global Q values are inconsistent with the large sSFR values because star formation activities are not likely to become aggressive in a gravitationally stable disk.

This inconsistency probably originates from the fact that the global Q parameter is not a reliable indicator for gas-rich galaxies (Romeo et al. 2010; Romeo & Agertz 2014). Instead, it can be important to investigate if the EMPGs lie on a tight relation based on observables such as the H I angular momentum (Romeo et al. 2020; Romeo 2020). We need high-resolution H I observations to discuss the gravitational instability of EMPGs precisely.

7.3. Connection to High-z Primordial Galaxies

The trend that $v_{\rm rot}/\sigma_0$ ($f_{\rm gas}$) decreases (increases) with decreasing (increasing) $12 + \log({\rm O/H})$ and M_* (sSFR) suggests that primordial galaxies at high redshifts would be dispersion-dominated gas-rich systems. This suggestion agrees with the decreasing trend of $v_{\rm rot}/\sigma_0$ with the redshift reported by both observational (e.g., Wisnioski et al. 2015) and simulation (Pillepich et al. 2019) studies.

Here, we investigate the kinematics of simulated primordial galaxies at high redshifts. In this study, we choose a $z = 7.3$ primordial galaxy of Wise et al. (2014)'s cosmological radiation hydrodynamics simulation because the simulated

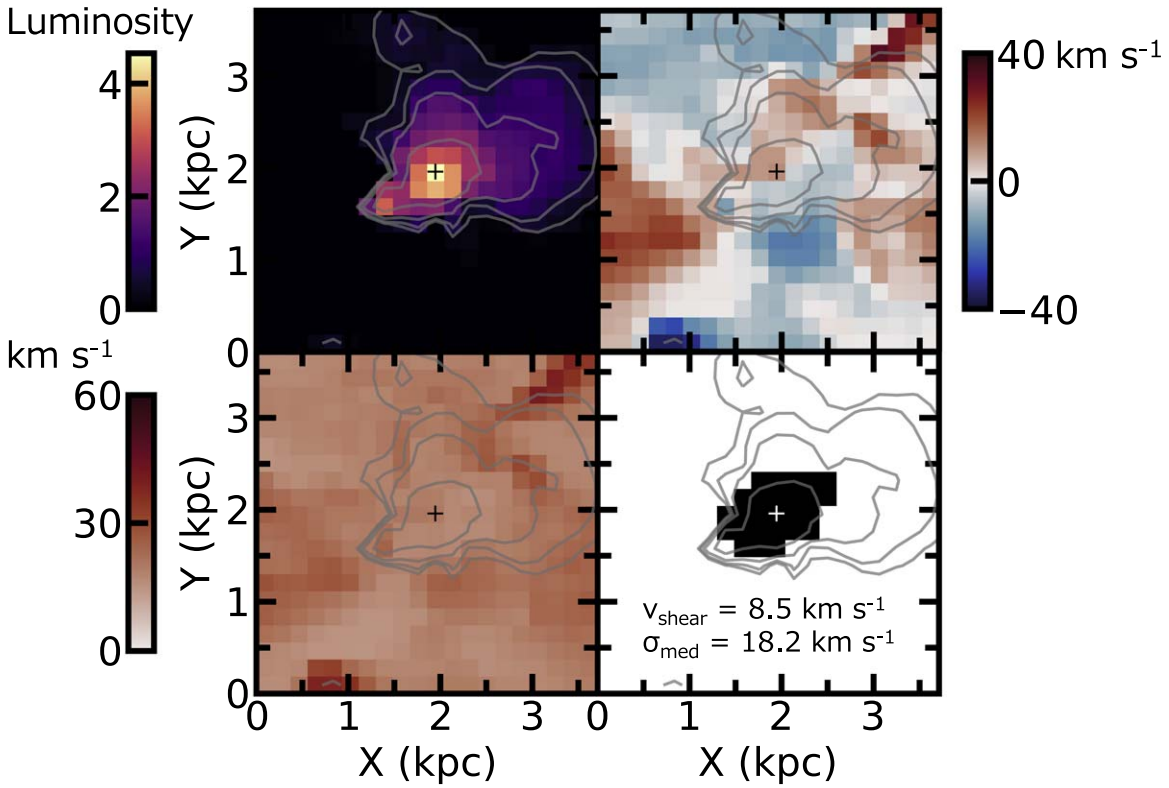

Figure 9. Hα luminosity (top left), velocity (top right), velocity dispersion (bottom left), and mask maps (bottom right) of the $z = 7.3$ primordial galaxy in Wise et al. (2014). The luminosity is in units of 10^{35} erg s^{-1} Å^{-1} in log scale. The maximum luminosity value (7×10^{39} erg s^{-1} Å^{-1}) corresponds to a flux of 3×10^{-15} erg s^{-1} cm^{-2} Å^{-1} at $z = 0.03125$. The gray contours illustrate Hα luminosity values of 1/16, 1/8, 1/4, and 1/2 of the maximum luminosity value.

galaxy has a low gas-phase metallicity (∼4% $Z_\odot$), a low stellar mass ($3.8 \times 10^6\,M_\odot$), a large $f_{\rm gas}$ (∼1), a large sSFR (∼5 Gyr^{-1}), and a small half-mass radius (∼200 pc), all of which are comparable[46] to those of the EMPGs (Sections 2 and 5.4.2). We extract the Hα flux, velocity, and velocity dispersion maps from the simulated galaxy. The FoV of the extracted region is 3.71 kpc with the spatial resolution of 3.71/252 = 0.015 kpc pixel^{-1}. The spectral resolution of the data cube is 0.1 Å. We use CLOUDY (Ferland et al. 2013) to derive the Hα fluxes from the following five quantities: hydrogen number density, temperature, metallicity, incident radiation intensity, and H I column density, along with enough parametric ranges and number of data points (1.8 million points in total). For each cell in the data cube of the five quantities, we linearly interpolate the emissivity table in 5D. To calculate the velocity map, We sum the line-of-sight velocities weighted by the Hα fluxes. To calculate the velocity dispersion map, we use the same method as Pillepich et al. (2019; Equation A3), using the Hα flux as the weights. We note that the velocity dispersions include thermal broadening.

We coarsen the data cube to a spatial resolution of 180 pc, similar to the resolution of our observations, to make a more relevant comparison. The top left, top right, and bottom left panels of Figure 9 are the Hα flux, velocity, and velocity dispersion maps of the simulated galaxy, respectively. We find that the simulated galaxy has an irregular morphology with multiple kinematic substructures and localized turbulent regions. These features can be seen in the EMPGs as well (Figure 4). Masking out the kinematic substructures and the turbulent regions, we also derive the kinematics properties of $v_{\rm shear}$ and $\sigma_{\rm med}$ in the same manner as we do for the EMPGs (Sections 5.1 and 5.2). We find that the simulated galaxy has a low $v_{\rm shear}$ (8.5 km s^{-1}) and a high $\sigma_{\rm med}$ (18.2 km s^{-1}), which are comparable to those of the EMPGs ($v_{\rm shear} = 5.5$–14.3 km s^{-1}, $\sigma_{\rm med} = 16.9$–30.8 km s^{-1}; see Section 6.1). Consequently, the simulated galaxy has a low $v_{\rm shear}/\sigma_{\rm med} = 0.47$ below unity suggesting that the simulated galaxy is dominated by dispersion as well as the EMPGs. Given that the local EMPGs, analogs of high-z primordial galaxies, and the simulated high-z primordial galaxies are both dispersion-dominated systems, we expect that high-z primordial galaxies are likely to be dispersion-dominated galaxies.

The forthcoming James Webb Space Telescope (JWST) can directly investigate the Hα kinematics of high-z primordial galaxies. Paper IV has simulated Hα fluxes of primordial galaxies with $M_* = 10^6\,M_\odot$ at redshifts ranging from 0 to 10. Comparing the Hα fluxes with the limiting flux of the JWST Near Infrared Spectrograph (NIRSpec), we estimate that NIRSpec can detect Hα fluxes of primordial galaxies with $M_* = 10^6\,M_\odot$ at $z \lesssim 1$ without gravitational lensing. With a ∼2 dex magnification from gravitational lensing, NIRSpec can detect Hα fluxes of primordial galaxies with $M_* = 10^6\,M_\odot$ at $z \sim 7$. We infer from this estimation that NIRSpec could observe primordial galaxies with $M_* \sim 10^7\,M_\odot$ at $z \sim 7$ with a realistic magnification of ∼1 dex. The top middle panel of Figure 8 shows that most of galaxies with $M_* \sim 10^7\,M_\odot$ already have low $v_{\rm rot}/\sigma_0 < 1$ and high $f_{\rm gas} > 0.5$. Lensing cluster surveys using the JWST such as GLASS (PI: T. Treu) and CANUCS (PI: C. Willott) will potentially pinpoint low-mass galaxies with $M_* \sim 10^7\,M_\odot$ at $z \sim 7$, and follow-up IFU

[46] Under the assumption that the half-mass radius is comparable to the rest-frame i-band effective radius.

observations with the JWST may identify dispersion-dominated gas-rich galaxies.

8. Summary

We present the kinematics of six local extremely metal-poor galaxies (EMPGs) with low metallicities ($0.016-0.098\,Z_{\odot}$) and low stellar masses ($10^{4.7}$–$10^{7.6}M_{\odot}$; Section 2). Taking deep medium/high-resolution ($R\sim7500$) integral-field spectra with the 8.2 m Subaru (Section 3), we resolve the small inner velocity gradients and dispersions of the EMPGs with Hα emission. Carefully masking out substructures originated by inflow and/or outflow, we fit three-dimensional disk models to the observed Hα flux, velocity, and velocity dispersion maps (Sections 4 and 5). All the EMPGs show rotational velocities ($v_{\rm rot}$) of 5–23 km s^{-1} smaller than the velocity dispersions (σ_0) of 17–31 km s^{-1}, indicating dispersion-dominated systems with small ratios of $v_{\rm rot}/\sigma_0=0.29$–$0.80$ (Section 6.1) that can be explained by turbulence driven by inflow and/or outflow (Section 7.1). Except for two EMPGs with large uncertainties, we find that the EMPGs have very large gas-mass fractions of $f_{\rm gas}\simeq0.9$–1.0 (Section 6.2). Comparing our results with other Hα kinematics studies, we find that $v_{\rm rot}/\sigma_0$ ($f_{\rm gas}$) decreases (increases) with decreasing metallicity. We compare numerical simulations of first-galaxy formation and identify that the simulated high-z ($z\sim7$) forming galaxies have gas fractions and dynamics similar to the observed EMPGs. Our EMPG observations and the simulations suggest that primordial galaxies are gas-rich dispersion-dominated systems, which would be identified by the forthcoming JWST observations at $z\sim7$ (Section 7.3).

Acknowledgments

We are grateful to Yoshiaki Sofue, Alessandro Romeo, and Roberto Terlevich for having useful discussions. We also thank the staff of Subaru Telescope for their help with the observations. This research is based on data collected at the Subaru Telescope, which is operated by the National Astronomical Observatory of Japan (NAOJ). We are honored and grateful for the opportunity of observing the universe from Maunakea, which has the cultural, historical, and natural significance in Hawaii. The Hyper Suprime-Cam (HSC) collaboration includes the astronomical communities of Japan and Taiwan, and Princeton University. The HSC instrumentation and software were developed by the NAOJ, the Kavli Institute for the Physics and Mathematics of the Universe (Kavli IPMU), the University of Tokyo, the High Energy Accelerator Research Organization (KEK), the Academia Sinica Institute for Astronomy and Astrophysics in Taiwan (ASIAA), and Princeton University. Based on data collected at the Subaru Telescope and retrieved from the HSC data archive system, which is operated by Subaru Telescope and Astronomy Data Center at NAOJ. This work was supported by the joint research program of the Institute for Cosmic Ray Research (ICRR), University of Tokyo. Y.I., K.N., Y.H., T.K., and M.O. are supported by JSPS KAKENHI grant Nos. 20H01895, 21K13909, and 21H05447. Y.H. is supported by JSPS KAKENHI grant Nos. 21J00153, 20K14532, 21H04499, 21K03614, and 22H01259. H.Y. is supported by MEXT/JSPS KAKENHI grant No. 21H04489 and JST FOREST Program grant No. JP-MJFR202Z. J.H.K acknowledges support from the National Research Foundation of Korea (NRF), grant Nos. 2020R1A2C3011091 and 2021M3F7A1084525, funded by the Korea government (MSIT). This work has been supported by the Japan Society for the Promotion of Science (JSPS) Grants-in-Aid for Scientific Research (19H05076 and 21H01128). This work has also been supported in part by the Sumitomo Foundation Fiscal 2018 Grant for Basic Science Research Projects (180923), and the Collaboration Funding of the Institute of Statistical Mathematics "New Development of the Studies on Galaxy Evolution with a Method of Data Science." The Cosmic Dawn Center is funded by the Danish National Research Foundation under grant No. 140. S.F. acknowledges support from the European Research Council (ERC) Consolidator Grant funding scheme (project ConTExt, grant No. 648179). This project has received funding from the European Union's Horizon 2020 research and innovation program under the Marie Sklodowska-Curie grant agreement No. 847523 "INTERACTIONS." This work is supported by World Premier International Research Center Initiative (WPI Initiative), MEXT, Japan, as well as KAKENHI Grant-in-Aid for Scientific Research (A) (15H02064, 17H01110, 17H01114, 20H00180, and 21H04467) through Japan Society for the Promotion of Science (JSPS). This work has been supported in part by JSPS KAKENHI grant Nos. JP17K05382, JP20K04024, and JP21H04499 (K. Nakajima). This research was supported by a grant from the Hayakawa Satio Fund awarded by the Astronomical Society of Japan. J.H.W. acknowledges support from NASA grants NNX17AG23G, 80NSSC20K0520, and 80NSSC21K1053 and NSF grants OAC-1835213 and AST-2108020.

Software: FOCAS IFU pipeline (Ozaki et al. 2020), PyRAF (Science Software Branch at STScI 2012), astropy (Astropy Collaboration et al. 2013; The Astropy Collaboration 2018), GalPaK^{3D} (Bouché et al. 2015), beagle (Chevallard & Charlot 2016), cloudy (Ferland et al. 2013), yt (Turk et al. 2011).

Appendix

Figures 10–14 show the GalPaK^{3D} fitting results of the five EMPGs other than J1631+4426.

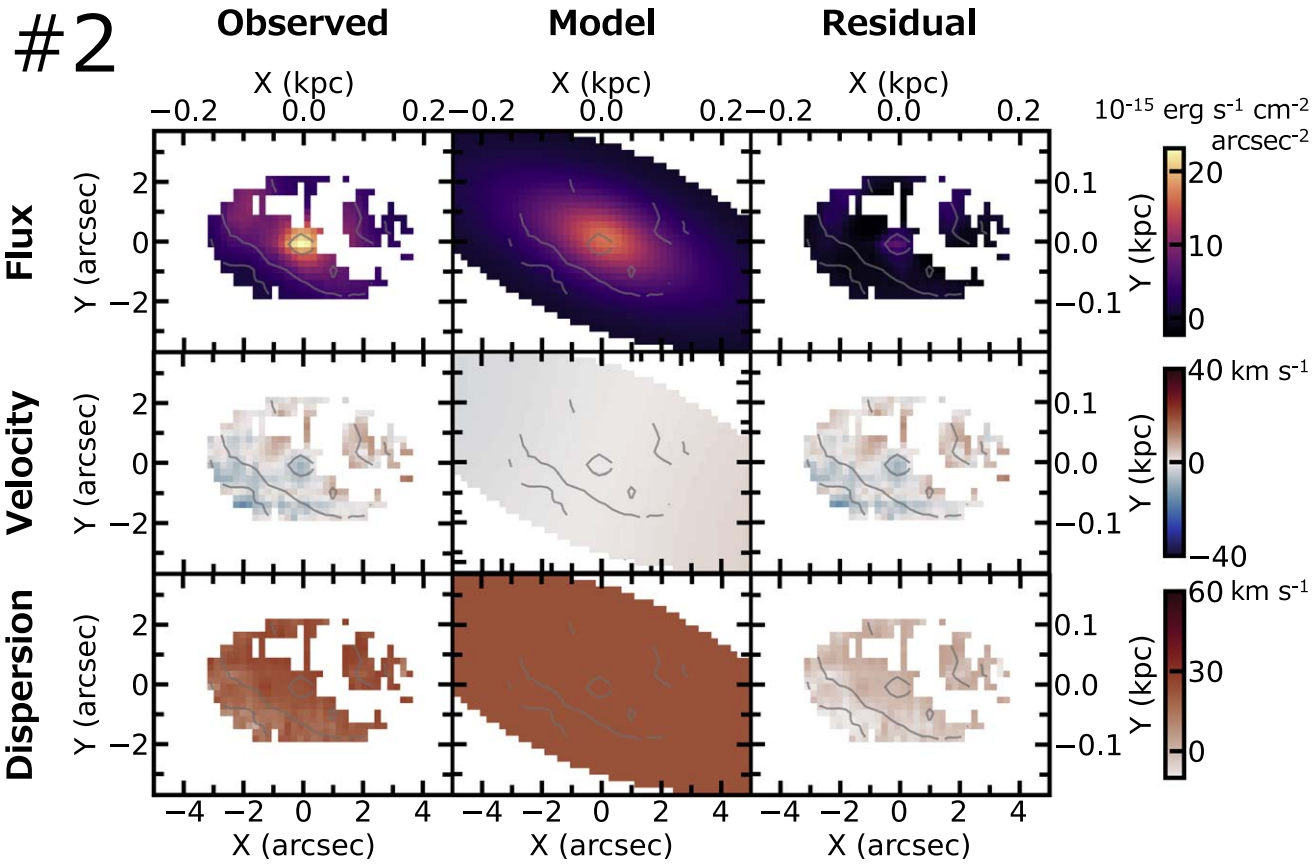

Figure 10. GalPaK^{3D} result of IZw18NW.

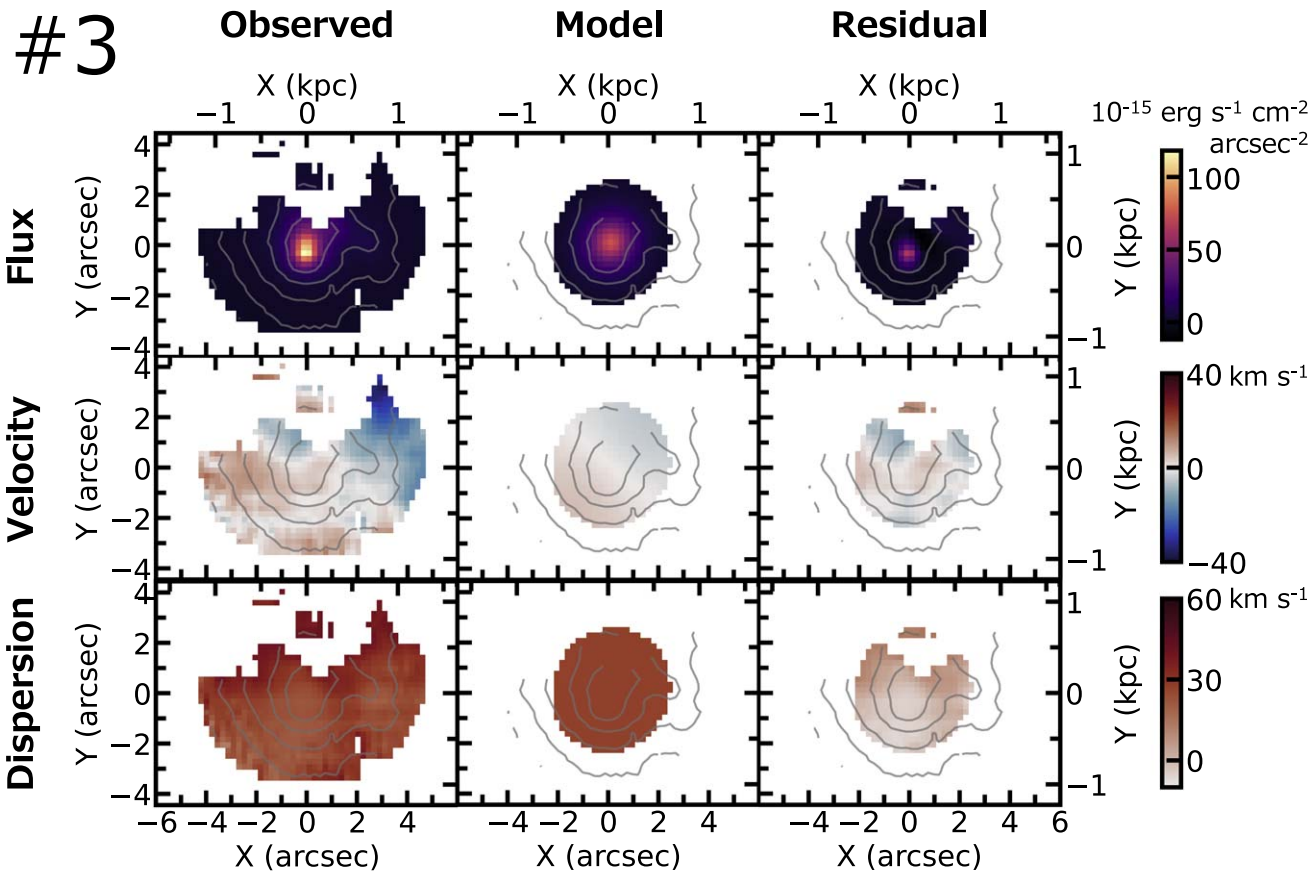

Figure 11. GalPaK^{3D} result of SBS0335−052E.

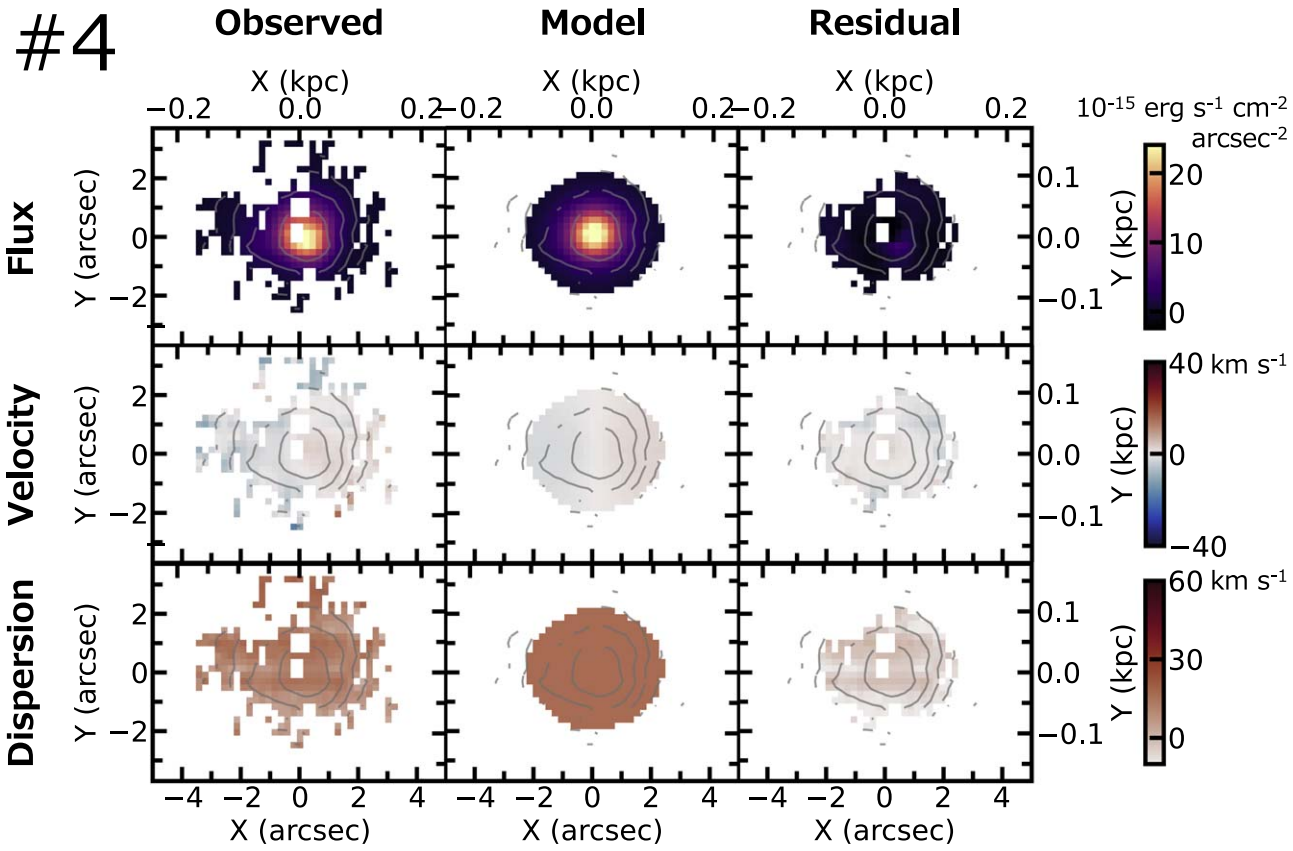

Figure 12. GalPaK^{3D} result of HS0822+3542.

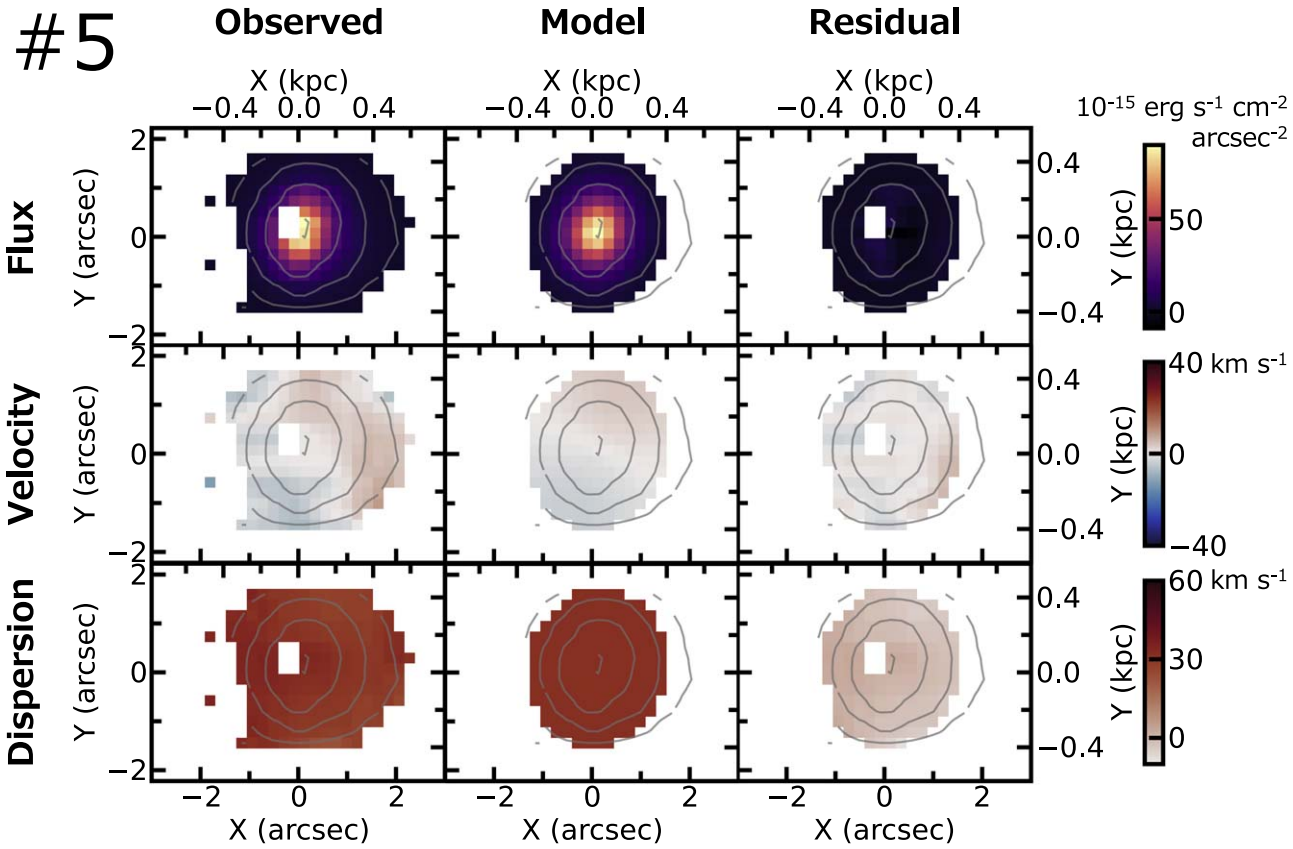

Figure 13. GalPaK^{3D} result of J1044+0353.

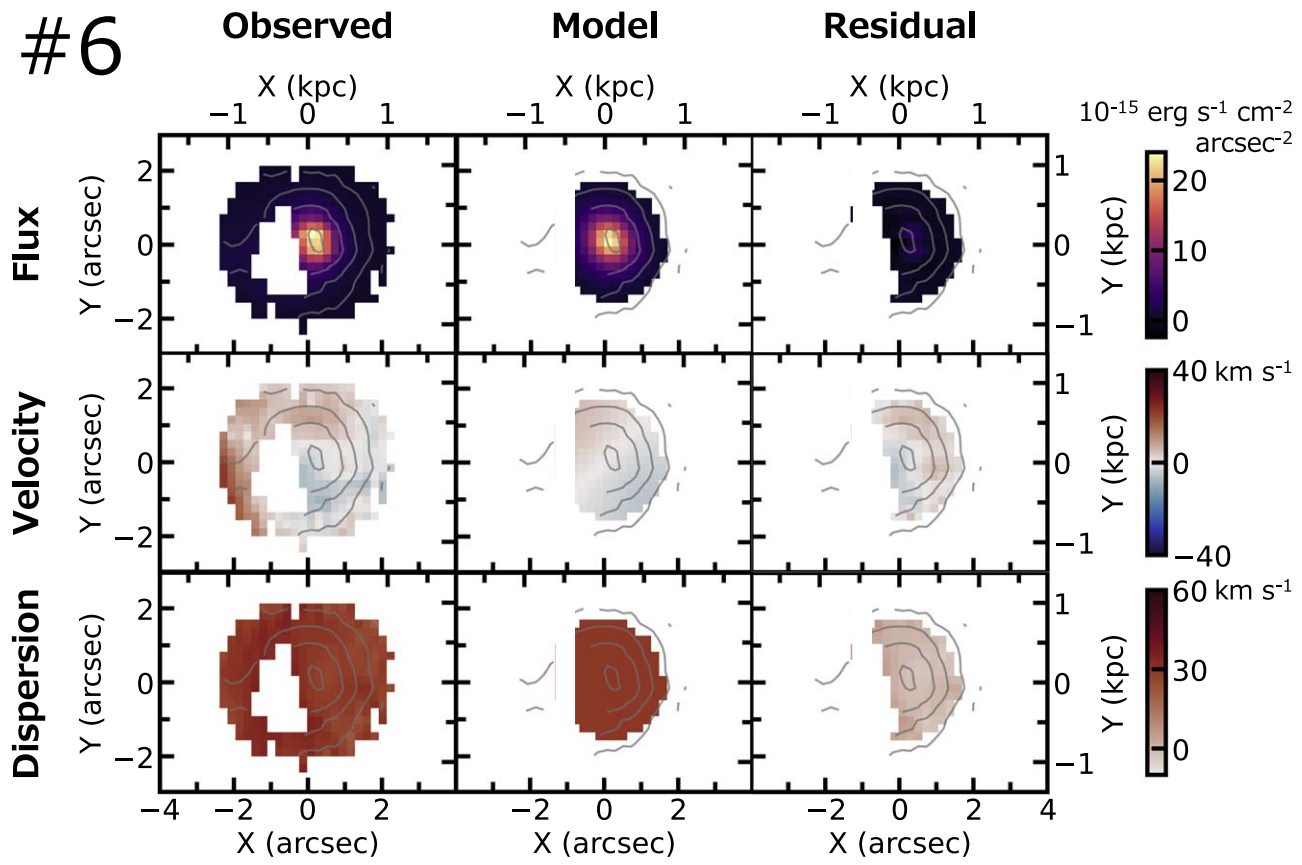

Figure 14. GalPaK^{3D} result of J2115−1734.

ORCID iDs

Yuki Isobe https://orcid.org/0000-0001-7730-8634
Masami Ouchi https://orcid.org/0000-0002-1049-6658
Kimihiko Nakajima https://orcid.org/0000-0003-2965-5070
Shinobu Ozaki https://orcid.org/0000-0002-5443-0300
Nicolas F. Bouché https://orcid.org/0000-0003-0068-9920
John H. Wise https://orcid.org/0000-0003-1173-8847
Yi Xu https://orcid.org/0000-0002-5768-8235
Eric Emsellem https://orcid.org/0000-0002-6155-7166
Haruka Kusakabe https://orcid.org/0000-0002-3801-434X
Takashi Hattori https://orcid.org/0000-0002-8996-7562
Tohru Nagao https://orcid.org/0000-0002-7402-5441
Gen Chiaki https://orcid.org/0000-0001-6246-2866
Hajime Fukushima https://orcid.org/0000-0002-0547-3208
Yuichi Harikane https://orcid.org/0000-0002-6047-430X
Kohei Hayashi https://orcid.org/0000-0002-8758-8139
Yutaka Hirai https://orcid.org/0000-0002-5661-033X
Ji Hoon Kim https://orcid.org/0000-0002-1418-3309
Michael V. Maseda https://orcid.org/0000-0003-0695-4414
Kentaro Nagamine https://orcid.org/0000-0001-7457-8487
Yuma Sugahara https://orcid.org/0000-0001-6958-7856
Hidenobu Yajima https://orcid.org/0000-0002-1319-3433
Shohei Aoyama https://orcid.org/0000-0002-1005-4120
Seiji Fujimoto https://orcid.org/0000-0001-7201-5066
Shun Hatano https://orcid.org/0000-0002-5816-4660
Akio K. Inoue https://orcid.org/0000-0002-7779-8677
Takashi Kojima https://orcid.org/0000-0001-5780-1886
Yutaka Komiyama https://orcid.org/0000-0002-3852-6329
Yusei Koyama https://orcid.org/0000-0002-0479-3699
Chien-Hsiu Lee https://orcid.org/0000-0003-1700-5740
Ken Mawatari https://orcid.org/0000-0003-4985-0201
Takashi J. Moriya https://orcid.org/0000-0003-1169-1954
Kentaro Motohara https://orcid.org/0000-0002-0724-9146
Kai Murai https://orcid.org/0000-0003-2879-1724
Moka Nishigaki https://orcid.org/0000-0003-4321-0975
Masato Onodera https://orcid.org/0000-0003-3228-7264
Yoshiaki Ono https://orcid.org/0000-0001-9011-7605
Michael Rauch https://orcid.org/0000-0002-1690-3488
Akihiro Suzuki https://orcid.org/0000-0002-7043-6112
Tsutomu T. Takeuchi https://orcid.org/0000-0001-8416-7673
Masayuki Umemura https://orcid.org/0000-0003-1615-1789
Kuria Watanabe https://orcid.org/0000-0002-2740-3403
Kiyoto Yabe https://orcid.org/0000-0001-6229-4858
Yechi Zhang https://orcid.org/0000-0003-3817-8739

References

Ahumada, R., Prieto, C. A., Almeida, A., et al. 2020, ApJS, 249, 3
Aihara, H., AlSayyad, Y., Ando, M., et al. 2019, PASJ, 71, 114
Aihara, H., AlSayyad, Y., Ando, M., et al. 2022, PASJ, 74, 247
Annibali, F., Cignoni, M., Tosi, M., et al. 2013, AJ, 146, 144
Asplund, M., Amarsi, A. M., & Grevesse, N. 2021, A&A, 653, A141
Aumer, M., Burkert, A., Johansson, P. H., & Genzel, R. 2010, ApJ, 719, 1230
Astropy Collaboration, Robitaille, T. P., Tollerud, E. J., et al. 2013, A&A, 558, A33
Bacon, R., Adam, G., Baranne, A., et al. 1995, A&AS, 113, 347
Barat, D., D'Eugenio, F., Colless, M., et al. 2019, MNRAS, 487, 2924
Barat, D., D'Eugenio, F., Colless, M., et al. 2020, MNRAS, 498, 5885

Berg, D. A., Skillman, E. D., Henry, R. B. C., Erb, D. K., & Carigi, L. 2016, ApJ, 827, 126
Bouché, N., Carfantan, H., Schroetter, I., Michel-Dansac, L., & Contini, T. 2015, AJ, 150, 92
Brinchmann, J., Charlot, S., White, S. D., et al. 2004, MNRAS,
Brook, C. B., Cintio, A. D., Knebe, A., et al. 2014, ApJL, 784, 1
Bruzual, G., & Charlot, S. 2003, MNRAS, 344, 1000
Chabrier, G. 2003, PASP, 115, 763
Chávez, R., Terlevich, R., Terlevich, E., et al. 2014, MNRAS, 442, 3565
Dib, S., Bell, E., & Burkert, A. 2006, ApJ, 638, 797
Chevallard, J., & Charlot, S. 2016, MNRAS, 462, 1415
Dufour, R. J., & Hester, J. J. 1990, ApJ, 350, 149
Dutton, A. A., & Macciò, A. V. 2014, MNRAS, 441, 3359
Egorov, O. V., Lozinskaya, T. A., Vasiliev, K. I., et al. 2021, MNRAS, 508, 2650
Ferland, G. J., Porter, R. L., van Hoof, P. A. M., et al. 2013, RMxAA, 49, 137
Flewelling, H. A., Magnier, E. A., Chambers, K. C., et al. 2020, ApJS, 251, 7
Förster Schreiber, N. M., Genzel, R., Bouché, N., et al. 2009, ApJ, 706, 1364
Fukushima, H., & Yajima, H. 2021, MNRAS, 506, 5512
Fukushima, H., & Yajima, H. 2022, MNRAS, 511, 3346
Geach, J. E., Smail, I., Moran, S. M., et al. 2011, ApJL, 730, L19
Genzel, R., Burkert, A., Bouché, N., et al. 2008, ApJ, 687, 59
Genzel, R., Newman, S., Jones, T., et al. 2011, ApJ, 733
Glazebrook, K. 2013, PASA, 30, e056
Green, A. W., Glazebrook, K., McGregor, P. J., et al. 2014, MNRAS, 437, 1070
Gutkin, J., Charlot, S., & Bruzual, G. 2016, MNRAS, 462, 1757
Herenz, E. C., Gruyters, P., Orlitova, I., et al. 2016, A&A, 587, A78
Herenz, E. C., Hayes, M., Papaderos, P., et al. 2017, A&A, 606, L11
Herrera-Camus, R., Förster Schreiber, N. M., Price, S. H., et al. 2022, A&A, 665, L8
Hirschauer, A. S., Salzer, J. J., Skillman, E. D., et al. 2016, ApJ, 822, 108
Hsyu, T., Cooke, R. J., Prochaska, J. X., & Bolte, M. 2017, ApJL, 845, L22
Isobe, Y., Ouchi, M., Kojima, T., et al. 2021, ApJ, 918, 54
Isobe, Y., Ouchi, M., Suzuki, A., et al. 2022, ApJ, 925, 111
Izotov, Y. I., Guseva, N. G., Fricke, K. J., & Papaderos, P. 2009, A&A, 503, 61
Izotov, Y. I., Lipovetsky, V. A., Chaffee, F. H., et al. 1997, ApJ, 476, 698
Izotov, Y. I., Stasińska, G., Meynet, G., Guseva, N. G., & Thuan, T. X. 2006, A&A, 448, 955
Izotov, Y. I., & Thuan, T. X. 1998, ApJ, 497, 227
Izotov, Y. I., Thuan, T. X., & Guseva, N. G. 2012, A&A,
Izotov, Y. I., Thuan, T. X., Guseva, N. G., & Liss, S. E. 2018, MNRAS, 473, 1956
Kashikawa, N., Aoki, K., Asai, R., et al. 2002, PASJ, 54, 819
Kashiwagi, Y., Inoue, A. K., Isobe, Y., et al. 2021, PASJ, 73, 1631
Kennicutt, R. C. J. 1998, ApJ, 498, 541
Kikuchihara, S., Ouchi, M., Ono, Y., et al. 2020, ApJ, 893, 60
Kniazev, A. Y., Grebel, E. K., Hao, L., et al. 2003, ApJL, 593, L73
Kniazev, A. Y., Pustilnik, S. A., Masegosa, J., et al. 2000, A&A, 357, 101
Kojima, T., Ouchi, M., Rauch, M., et al. 2020, ApJ, 898, 142
Kojima, T., Ouchi, M., Rauch, M., et al. 2021, ApJ, 913, 22
Krumholz, M. R. 2013, MNRAS, 436, 2747
Krumholz, M. R., Burkhart, B., Forbes, J. C., & Crocker, R. M. 2018, MNRAS, 477, 2716
Kunth, D., & Östlin, G. 2000, A&ARv, 10, 1
Law, D. R., Steidel, C. C., Erb, D. K., et al. 2009, ApJ, 697, 2057
Lehnert, M. D., Nesvadba, N. P. H., Le Tiran, L., et al. 2009, ApJ, 699, 1660
Lelli, F., Verheijen, M., Fraternali, F., & Sancisi, R. 2012, A&A, 537, A72
Mac Low, M.-M., & Klessen, R. S. 2004, RvMP, 76, 125
Maseda, M. V., van der Wel, A., Rix, H.-W., et al. 2014, ApJ, 791, 17
Matsumoto, A., Ouchi, M., Nakajima, K., et al. 2022, ApJ, 941, 167
Miyazaki, S., Komiyama, Y., Kawanomoto, S., et al. 2018, PASJ,
Moiseev, A. V., Pustilnik, S. A., & Kniazev, A. Y. 2010, MNRAS, 405, 2453
Morales-Luis, A. B., Sánchez Almeida, J., Aguerri, J. A. L., & Muñoz-Tuñón, C. 2011, ApJ, 743, 77
Nakajima, K., Ouchi, M., Xu, Y., et al. 2022, ApJS, 262, 3
Navarro, J. F., Frenk, C. S., & White, S. D. M. 1996, ApJ, 462, 563
Oke, J. B., & Gunn, J. E. 1983, ApJ, 266, 713
Ostriker, E. C., McKee, C. F., & Leroy, A. K. 2010, ApJ, 721, 975
Ozaki, S., Fukushima, M., Iwashita, H., et al. 2020, PASJ, 72, 97
Papaderos, P., Guseva, N. G., Izotov, Y. I., & Fricke, K. 2008, A&A, 491, 113
Pillepich, A., Nelson, D., Springel, V., et al. 2019, MNRAS, 490, 3196
Prole, D. J., Hilker, M., van der Burg, R. F. J., et al. 2019, MNRAS, 484, 4865
Pustilnik, S. A., Brinks, E., Thuan, T. X., Lipovetsky, V. A., & Izotov, Y. I. 2001, AJ, 121, 1413
Pustilnik, S. A., Egorova, E. S., Kniazev, A. Y., et al. 2021, MNRAS, 507, 944
Pustilnik, S. A., Egorova, E. S., Perepelitsyna, Y. A., & Kniazev, A. Y. 2020a, MNRAS, 492, 1078
Pustilnik, S. A., Kniazev, A. Y., Perepelitsyna, Y. A., & Egorova, E. S. 2020b, MNRAS, 493, 830
Pustilnik, S. A., Kniazev, A. Y., & Pramskij, A. G. 2005, A&A, 443, 91
Romeo, A. B. 2020, MNRAS, 491, 4843
Romeo, A. B., & Agertz, O. 2014, MNRAS, 442, 1230
Romeo, A. B., Agertz, O., & Renaud, F. 2020, MNRAS, 499, 5656
Romeo, A. B., Burkert, A., & Agertz, O. 2010, MNRAS, 407, 1223
Science Software Branch at STScI 2012, PyRAF: Python alternative for IRAF, Astrophysics Source Code Library, ascl:1207.011
Searle, L., & Sargent, W. L. W. 1972, ApJ, 173, 25
Shi, Y., Armus, L., Helou, G., et al. 2014, Natur, 514, 335
Skillman, E. D., Salzer, J. J., Berg, D. A., et al. 2013, AJ, 146, 3
The Astropy Collaboration 2018, astropy v3.1: a core python package for astronomy, v3.1, Zenodo, doi: 10.5281/zenodo.4080996
Thuan, T. X., Izotov, Y. I., & Lipovetsky, V. A. 1997, ApJ, 477, 661
Tody, D. 1986, Proc. SPIE, 627, 733
Toomre, A. 1964, ApJ, 139, 1217
Tremonti, C. A., Heckman, T. M., Kauffmann, G., et al. 2004, ApJ, 613, 898
Turk, M. J., Smith, B. D., Oishi, J. S., et al. 2011, ApJS, 192, 9
Umeda, H., Ouchi, M., Nakajima, K., et al. 2022, ApJ, 930, 37
Wise, J. H., Demchenko, V. G., Halicek, M. T., et al. 2014, MNRAS, 442, 2560
Wise, J. H., Turk, M. J., Norman, M. L., & Abel, T. 2012, ApJ, 745, 50
Wisnioski, E., Förster Schreiber, N. M., Wuyts, S., et al. 2015, ApJ, 799, 209
Xu, Y., Ouchi, M., & Isobe, Y. 2023, arXiv:2303.12467
Xu, Y., Ouchi, M., Rauch, M., et al. 2022, ApJ, 929, 134
Yajima, H., Abe, M., Khochfar, S., et al. 2022, MNRAS, 509, 4037